Adiabatic evolution of asymmetric binaries on generic orbits with new fundamental fields I: Characterization of gravitational wave fluxes

Sara Gliorio,[1,2,*] Matteo Della Rocca,[3,4,5,†] Susanna Barsanti,[6,‡] Leonardo Gualtieri,[4,7,§] Andrea Maselli,[1,2,‖] and Thomas P. Sotiriou[8,9,¶]

[1]*Gran Sasso Science Institute (GSSI), I-67100 L'Aquila, Italy*
[2]*INFN, Laboratori Nazionali del Gran Sasso, I-67100 Assergi, Italy*
[3]*Dipartimento di Fisica, Sapienza Università di Roma, Piazzale Aldo Moro 5, 00185 Rome, Italy*
[4]*Dipartimento di Fisica, Università di Pisa, Largo Bruno Pontecorvo 3, 56127 Pisa, Italy*
[5]*INFN, Sezione di Roma, Piazzale Aldo Moro 2, 00185 Rome, Italy*
[6]*School of Mathematics and Statistics, University College Dublin, Belfield, Dublin 4, Ireland*
[7]*INFN, Sezione di Pisa, Largo Bruno Pontecorvo 3, 56127 Pisa, Italy*
[8]*School of Mathematical Sciences and School of Physics and Astronomy, University of Nottingham, University Park, Nottingham, NG7 2RD, United Kingdom*
[9]*Nottingham Centre of Gravity, University of Nottingham, University Park, Nottingham, NG7 2RD, United Kingdom*

(Received 23 March 2026; accepted 29 June 2026; published 1 September 2026)

We investigate the dynamics of asymmetric binaries in extensions of general relativity (GR) featuring a massless scalar field nonminimally coupled to gravity, focusing on the interplay between eccentricity and inclination in fully generic bound orbits. Building on an effective field theory framework tailored to extreme- and intermediate-mass-ratio inspirals, we compute scalar-field perturbations using a new arbitrary-precision C++ code capable of evolving perturbations along generic Kerr geodesics, STORM. We investigate the complete set of scalar fluxes at infinity and through the horizon across the relevant parameter space and analyze their harmonic structure as a function of orbital geometry and black-hole spin. Our results advance ongoing efforts to construct accurate waveform models for asymmetric binaries beyond GR and lay the groundwork for precision tests of fundamental physics with next-generation gravitational-wave detectors.

DOI: 10.1103/b3lv-8r4p

I. INTRODUCTION

We are now more than a decade into the gravitational-wave (GW) era. Laser Interferometer Gravitational-Wave Observatory (LIGO), Virgo, and Kamioka Gravitational Wave Detector (KAGRA) (LVK) have detected more than 200 events, reshaping our view of the Universe and revealing the dynamics of black holes (BHs) in the highly dynamical, strong-field regime of compact binary coalescences [1]. These observations have transformed GW sources into unparalleled laboratories for fundamental physics [2]. Ground-based interferometers have also enabled searches for new physics beyond general relativity (GR) or the Standard Model using comparable-mass binaries with mass ratios up to $\epsilon = m_2/m_1 \sim 1/10$ [3,4], and have already placed stringent constraints on deviations from GR [5–7].

The coming decade—driven by the advent of next-generation detectors on the ground [8,9] and in space [10–12], together with the ambitious science goals of facilities such as the Einstein Telescope and Laser Interferometer Space Antenna (LISA) [13–17]—promises a transformative leap in GW astronomy. These instruments will detect sources across a far broader mass spectrum, including populations that remain dim to current interferometers.

Among the most compelling targets are asymmetric binaries with mass ratios $\epsilon \sim 10^{-7} - 10^{-2}$, such as extreme- and intermediate-mass-ratio inspirals (EMRIs/IMRIs). Composed of stellar-mass compact objects inspiraling into massive BHs, these systems can be tracked for hundreds of thousands of orbital cycles—often on highly relativistic, inclined, and eccentric trajectories—within the LISA band.

*Contact author: sara.gliorio@gssi.it
†Contact author: matteo.dellarocca@uniroma1.it
‡Contact author: susanna.barsanti@ucd.ie
§Contact author: leonardo.gualtieri@unipi.it
‖Contact author: andrea.maselli@gssi.it
¶Contact author: Thomas.Sotiriou@nottingham.ac.uk

Published by the American Physical Society under the terms of the Creative Commons Attribution 4.0 International license. Further distribution of this work must maintain attribution to the author(s) and the published article's title, journal citation, and DOI.

Their rich harmonic structure and extended signal duration enable subpercent precision in parameter estimation [18,19].

While asymmetric binaries are exceptionally promising for fundamental-physics tests [15,20–34], modeling them remains a substantial challenge.

Robust tests of gravity require accurate theoretical predictions of BH dynamics and their GW emission both within GR and in extensions beyond GR. The self-force (SF) framework provides the leading methodology for modeling asymmetric binaries in GR, leveraging the small mass ratio as an expansion parameter within relativistic perturbation theory [35–38]. Extending these models beyond GR is considerably more demanding, owing to additional fields, new couplings, and the absence of a Kerr-like solution that could serve as the background spacetime for perturbative analyses. Progress in this direction has been made recently, with Refs. [39,40] developing a formalism that generalizes Teukolsky's equation to modified theories of gravity.

Effective field theory (EFT) methods have emerged as a powerful toolkit for studying BH dynamics in extensions of GR. Recent work [41] has applied this approach to asymmetric binaries, exploiting their intrinsic mass hierarchy to model their evolution in a broad class of theories featuring massless scalar fields nonminimally coupled to gravity, and showing that deviations from the Kerr geometry of the primary are negligible at leading order in the mass ratio, while the scalar charge of the secondary fully determines the departure from GR. This enables the construction of adiabatic-order waveforms that remain modularly adaptable to existing GR templates and introduce only one new parameter, the scalar charge d of the secondary BH. The same framework has been embedded within a genuine SF formalism to compute postadiabatic corrections to the binary dynamics [42].

This analysis—which for brevity we shall call the EFT approach—has been extended to a variety of orbital configurations, including equatorial eccentric [43,44] and spherical inclined [45] trajectories, as well as to fully generic bound inspirals in recent analyses focused on the evolution of EMRIs on arbitrary orbits [46]. In parallel, a complementary line of work has applied SF methods to model not only the inspiral but also the merger and ringdown in theories beyond GR, under the small-mass-ratio approximation [47]. Additional theoretical progress has explored the impact of massive scalar fields using the EFT approach in the context of circular orbits [48], time-dependent scalar charges [49], and has further extended the framework to vector fields, for circular and eccentric [50–52] trajectories. The EFT approach has also been exploited to show that the scalar charge of the secondary can imprint strong, detectable signatures on EMRI waveforms [53,54]. Finally, scalar self-force studies were also carried out for equatorial circular [55], equatorial eccentric [56], spherical inclined [57], and generic orbits [58].

In this paper, we take a step further by generalizing the framework introduced in Ref. [41] to describe the dynamics of asymmetric binaries on fully generic orbits, simultaneously incorporating eccentricity and inclination in the presence of massless scalar fields. To achieve this, we integrate the scalar-field perturbation equations using Scalar Tensor Orbital Radiation from EMRIs (STORM) [59], a new C++ code which computes perturbations along generic bound geodesics with arbitrary-precision numerics. We characterize, for the first time within this framework, the full spectrum of scalar fluxes emitted at the horizon and at infinity as a function of the orbital parameters and the BH spin. We examine in detail the structure and properties of their harmonic content, analyzing the relative weight of each mode in the overall flux emitted by the binary.

These developments complement ongoing efforts to model compact-binary dynamics and waveforms beyond GR and contribute to a broader program aimed at enabling precision tests of fundamental physics with asymmetric binaries. The present work is intended as a foundational element of this program, providing both the theoretical framework and numerical infrastructure upon which more complete beyond-GR waveform models can be built.

In Sec. II, we review the theoretical framework. In Sec. III, we discuss our results. Finally, in Sec. IV, we draw our conclusions. Throughout the paper we use geometric $G = c = 1$ units.

II. THEORETICAL SETUP

In this section, we detail the theoretical formalism used to compute the scalar-led and gravitational-led fluxes along generic orbits. We begin by describing the classes of beyond-GR models we consider, discussing then how to determine the equations of perturbations at the adiabatic order.

A. Scalar fields and EMRIs

We consider a general action describing a nonminimally coupled, real, and massless scalar field ψ [42], as follows:

$$S[\mathbf{g},\psi,\Psi] = S_0[\mathbf{g},\psi] + \alpha S_{\rm c}[\mathbf{g},\psi] + S_{\rm m}[\mathbf{g},\psi,\Psi], \quad (1)$$

where $\mathbf{g}$ denotes the spacetime metric, S_0 is the GR action

$$S_0 = \int \mathrm{d}^4x \frac{\sqrt{-g}}{16\pi}\left(R - \frac{1}{2}\partial_\mu\psi\partial^\mu\psi\right), \quad (2)$$

and R is the Ricci scalar. The nonminimal coupling between the scalar field and the metric is encoded in the term $\alpha S_{\rm c}$, where the coupling constant α has dimensions, in geometrized units, $(\text{mass})^N$. Matter fields, denoted by Ψ, are described by the action $S_{\rm m}$. In our setup, we assume that either $\alpha = 0$, i.e., the contribution $\alpha S_{\rm c}$ vanishes, or α has dimensions $N > 1$, defining in physical units a characteristic energy scale above which interactions are suppressed. This choice includes the vast majority of scalar-tensor

gravity theories that are currently of interest, including Bergmann-Wagoner theories (for which $\alpha = 0$), all shift-symmetric Horndeski theories that admit Minkowski as a solution [60], as well as all known scalarization models [61–66].[1]

Varying the action (1) with respect to the field content yields the equations of motion:

$$G_{\mu\nu} = 8\pi T^{\rm scal}_{\mu\nu} + \alpha T^{\rm c}_{\mu\nu} + T^{\rm m}_{\mu\nu}, \qquad \Box\psi = \alpha T^{\rm c} + T^{\rm m}, \quad (3)$$

where $\Box = \nabla_\mu\nabla^\mu$, $T^{\rm scal}_{\mu\nu} = \frac{1}{16\pi}[\partial_\mu\psi\partial_\nu\psi - \frac{1}{2}g_{\mu\nu}(\partial\psi)^2]$, and

$$T^{\rm c}_{\mu\nu} = -\frac{16\pi}{\sqrt{-g}}\frac{\delta S_{\rm c}}{\delta g^{\mu\nu}}, \qquad T^{\rm m} = -\frac{16\pi}{\sqrt{-g}}\frac{\delta S_{\rm m}}{\delta\psi}. \quad (4)$$

Solving for the metric and scalar field requires addressing the coupled system (3). However, the mass asymmetry characteristic of EMRIs naturally simplifies the problem, allowing tensor and scalar perturbations to decouple at leading dissipative order in the mass ratio. A rigorous treatment of this decoupling within an SF framework, including postadiabatic corrections, was developed in Ref. [42], to which we refer for details. Here, we present the fundamental equations governing the leading-order perturbations and their application to generic orbits.

We consider binaries in which the primary is a BH of mass M, and the secondary a compact object of mass $m_{\rm p} \ll M$. Thus, the field equations (3) can be solved perturbative in the mass ratio $\epsilon = m_{\rm p}/M \ll 1$. Moreover, this choice leads to a hierarchy of scales, in which the secondary body, with a typical length-scale $\sim m_{\rm p}$, moves in the "exterior" spacetime of the primary, with the larger length-scale $\sim M$. We can then use an EFT (or "skeletonized") approach [69–71], in which the matter action is replaced by the particle action

$$S_{\rm p} = -\int_\gamma m(\psi)\sqrt{g_{\mu\nu}\frac{{\rm d}y^\mu_{\rm p}}{{\rm d}\tau}\frac{{\rm d}y^\nu_{\rm p}}{{\rm d}\tau}}{\rm d}\tau, \quad (5)$$

where γ: $\tau \to y^\mu_{\rm p}(\tau)$ is the worldline of the secondary body, in a coordinate system $\{y^\mu\}$. In the length-scale of the exterior spacetime, the secondary body is treated as a pointlike object, and the function $m(\psi)$—encoding the coupling of the body with the scalar field—is evaluated at its location.

When $\alpha = 0$, the exterior spacetime is solution to the Einstein-Klein-Gordon field equations and thus, due to no-hair theorems [72–76] is described by the Kerr metric with a constant scalar field. When $\alpha \neq 0$, assuming that for $\alpha \to 0$ the solutions of Eq. (3) are continuously connected to GR, any corrections to the Kerr metric must depend on the dimensionless parameter

$$\zeta = \frac{\alpha}{M^N} = \epsilon^N\frac{\alpha}{m_{\rm p}^N}, \quad (6)$$

where, as discussed above, we are assuming $N > 1$. Astrophysical observations in both GW and electromagnetic spectra for stellar-mass sources constrain $\alpha/m_{\rm p}^N \lesssim \mathcal{O}(1)$ [6,7,77–80]. Therefore, $\zeta \lesssim \epsilon^N \ll 1$, implying that deviations from the Kerr background can be safely neglected at leading adiabatic order, and the background scalar field is constant due to no-hair theorems. Crucially, Eq. (6) also allows us to use ϵ as a single bookkeeping parameter to describe both metric and scalar perturbations, as in the gravitational SF formalism in GR:

$$g_{\mu\nu} = g^{(0)}_{\mu\nu} + \epsilon h^{(1)}_{\mu\nu} + \ldots, \quad \psi = \psi^{(0)} + \epsilon\psi^{(1)} + \ldots. \quad (7)$$

At zeroth order in the mass ratio, the background spacetime $g^{(0)}_{\mu\nu}$ is the Kerr metric, and the scalar field $\psi^{(0)}$, arising from S_0, is constant and can be set to zero without loss of generality.

The first-order perturbations, $h^{(1)}_{\mu\nu}$ and $\psi^{(1)}$, corresponding to the leading dissipative SF contribution, are sourced by the secondary object. In the field equations (3), the contributions of $T^{\rm scal}_{\mu\nu}$ and $\delta S_{\rm c}/\delta\psi$, which are at least quadratic in ϵ, can be neglected. Since $m_{\rm p} \ll M$, there exists a buffer region inside the world tube of the secondary object where the scalar field admits a multipolar decomposition. In a local coordinate frame $\{\tilde{x}_\mu\}$ centered on the secondary, this region is determined by the condition $m_{\rm p} \ll \tilde{r} \ll M$, where $\tilde{r}$ is the spatial distance from the worldline of the secondary. Within this region, the scalar field solution is

$$\psi^{(1)} = \frac{m_{\rm p}d}{\tilde{r}} + \mathcal{O}(m_{\rm p}^2/\tilde{r}^2), \quad (8)$$

where the dimensionless constant d is called the *scalar charge* of the secondary body, and measures the leading monopole term in the scalar multipolar expansion. Note that d is not a conserved, Noether charge.

Substituting the expansion (8) into the scalar field equation yields the matching conditions, as follows:

$$m_{\rm p} = m(\psi)|_{\psi=0}, \qquad d = -4\frac{m'(\psi)}{m_{\rm p}}\bigg|_{\psi=0}. \quad (9)$$

Expanding the field equations (3) at linear order in ϵ, with the source term given by $S_{\rm p}$, yields decoupled equations for the metric and scalar perturbations, as follows:

[1]Chern-Simons gravity [67] is also formally covered by our action if one takes ϕ to be a pseudoscalar. However, in that case, the scalar charge is dipolar [68], which will not be covered by our analysis of the particle action below.

$$G^{\alpha\beta}[h^{(1)}_{\alpha\beta}] = 8\pi m_{\rm p}\int \frac{\delta^{(4)}(x-y_{\rm p}(\tau))}{\sqrt{-g}}\frac{{\rm d}y^{\alpha}_{\rm p}}{{\rm d}\tau}\frac{{\rm d}y^{\beta}_{\rm p}}{{\rm d}\tau}{\rm d}\tau, \quad (10)$$

$$\Box\psi^{(1)} = -4\pi d m_{\rm p}\int \frac{\delta^{(4)}(x-y_{\rm p}(\tau))}{\sqrt{-g}}{\rm d}\tau, \quad (11)$$

where

$$G^{\mu\nu}[h^{(1)}_{\alpha\beta}] = \frac{\rm d}{{\rm d}\lambda}G_{\mu\nu}[g^{(0)}_{\alpha\beta}+\lambda h^{(1)}_{\alpha\beta}]\Big|_{\lambda=0} \quad (12)$$

is the linearized Einstein operator acting on $h_{\alpha\beta}$. Equations (10) coincide with those of GR, leading to the Teukolsky equations for Kerr perturbations. The scalar field equation, by contrast, contains an integral encoding the orbital dynamics of the secondary and depends on the scalar charge d, which sets the overall amplitude of $\psi^{(1)}$.

The field equations (10)–(11) show that at leading order in the mass ratio ϵ, the dynamics depend on the underlying modified theory of gravity only through the scalar charge d appearing in the source term of Eq. (11). Any dependence on the fundamental coupling α entering the interaction sector $S_{\rm c}$ is therefore encoded implicitly in the relation between the coupling α and the scalar charge d. As discussed in Ref. [41], this property makes the framework completely agnostic with respect to the expression of the interaction terms included in $S_{\rm c}$.

This observation has important practical consequences. At leading order in the mass ratio, waveform modeling and data analysis can be performed directly in terms of the phenomenological parameter d, without specifying a particular modified theory of gravity. In the remainder of this work, we therefore treat d as the fundamental parameter controlling beyond-GR effects.

Once a specific theory is selected, measurements or constraints on d can be translated into measurements or constraints on the corresponding fundamental coupling through the theory-dependent relation $d = d(\alpha)$. For example, in shift-symmetric scalar Gauss-Bonnet gravity, for BHs regularity, conditions at the horizon fix d to depend on the BH mass and on the fundamental coupling as $d \propto \alpha/M^2_{\rm BH}$, with a proportionality coefficient of order unity [81–83]. Therefore, any observational bound on d can be immediately reinterpreted as a bound on α. Analogous mappings can be constructed for other theories once the corresponding relation between the scalar charge and the fundamental couplings is known.

B. Orbital motion

At adiabatic order, the trajectory of a small compact object during inspiral follows a sequence of geodesics around the primary, described by the Kerr metric. In Boyer-Lindquist coordinates $x^{\mu} = (t, r, z = \cos\theta, \phi)$, the line element reads

$$\begin{aligned}{\rm d}s^2 = &-\left(1-\frac{2Mr}{\Sigma}\right){\rm d}t^2 - \frac{4Mar(1-z^2)}{\Sigma}{\rm d}t{\rm d}\phi \\ &+\frac{\Sigma}{\Delta}{\rm d}r^2 + \frac{\Sigma}{1-z^2}{\rm d}z^2 + \frac{1-z^2}{\Sigma}[2Ma^2r(1-z^2) \\ &+(a^2+r^2)\Sigma]{\rm d}\phi^2, \end{aligned} \quad (13)$$

where $j = aM$ is the BH angular momentum, and

$$\begin{aligned}\Delta &= r^2 - 2Mr + a^2 = (r-r_+)(r-r_-), \\ \Sigma &= r^2 + a^2z^2,\end{aligned}$$

with $r_{\pm} = M \pm \sqrt{M^2-a^2}$, and $\pm$ denoting the inner and outer horizons.

Geodesics in Kerr spacetime admit four conserved quantities: the normalization of the four-velocity $u^{\mu} = {\rm d}x^{\mu}/{\rm d}\tau$ ($u_{\mu}u^{\mu} = -1$), the specific energy $\mathcal{E}$, the azimuthal angular momentum $\mathcal{L}$, and the Carter constant $\mathcal{Q}$, the latter arising from the Killing tensor $\mathcal{K}_{\mu\nu}$ [84], as follows:

$$\mathcal{E} = -g_{tt}\dot{t} - g_{t\phi}\dot{\phi} \quad (14)$$

$$\mathcal{L} = g_{\phi t}\dot{t} + g_{\phi\phi}\dot{\phi}, \quad (15)$$

$$\mathcal{Q} = u^{\mu}\mathcal{K}_{\mu\nu}u^{\nu} - (\mathcal{L}-a\mathcal{E})^2. \quad (16)$$

With these conserved quantities, the geodesic equations take the form [85]

$$\begin{aligned}\left(\frac{{\rm d}r}{{\rm d}\lambda}\right)^2 &= R(r) \\ &= [\mathcal{E}(r^2+a^2) - a\mathcal{L}]^2 \quad (17)\\ &\quad -\Delta[r^2 + (\mathcal{L}-a\mathcal{E})^2 + \mathcal{Q}], \quad (18)\end{aligned}$$

$$\begin{aligned}\left(\frac{{\rm d}z}{{\rm d}\lambda}\right)^2 &= \Theta(z) \\ &= \mathcal{Q} - z^2[a^2(1-\mathcal{E}^2)(1-z^2) + \mathcal{L}^2 + \mathcal{Q}], \end{aligned} \quad (19)$$

$$\begin{aligned}\frac{{\rm d}t}{{\rm d}\lambda} &= T(r,z) \\ &= \mathcal{E}\left[\frac{(r^2+a^2)^2}{\Delta} - a^2(1-z^2)\right] \\ &\quad + a\mathcal{L}\left(1-\frac{r^2+a^2}{\Delta}\right), \end{aligned} \quad (20)$$

$$\begin{aligned}\frac{{\rm d}\phi}{{\rm d}\lambda} &= \Phi(r,z) \\ &= \frac{\mathcal{L}}{1-z^2} + a\mathcal{E}\left(\frac{r^2+a^2}{\Delta}-1\right) - \frac{a^2\mathcal{L}}{\Delta}, \end{aligned} \quad (21)$$

where τ is the proper time and λ the Mino time [86], defined by $\mathrm{d}\lambda = \mathrm{d}\tau/\Sigma$. We focus on bound orbits, characterized by $0 \le \mathcal{E} < 1$ and $\mathcal{Q} \ge 0$ [87].

The radial potential $R(r)$ is a quartic polynomial that factorizes as

$$R(r) = (1-\mathcal{E}^2)(r_1 - r)(r - r_2)(r - r_3)(r - r_4), \quad (22)$$

with roots $r_4 \le r_3 \le r_2 \le r_1$. The radial motion is confined between the turning points $r_2 \le r \le r_1$. Similarly, the polar potential can be written as

$$\Theta(z) = (z^2 - z_1^2)[a^2(1-\mathcal{E}^2)z^2 - z_2^2], \quad (23)$$

so that the motion in z is bounded between $\pm z_1$, corresponding to polar angles $\theta_{\min} = \arccos|z_1|$ and $\theta_{\max} = \pi - \theta_{\min}$. Both radial and polar motions are periodic, with fundamental periods Λ_r and Λ_z in Mino time such that

$$y^i(\lambda + \Lambda_i) = y^i(\lambda), \qquad i \in \{r, z\}. \quad (24)$$

Introducing angle variables[2]

$$q_r = \lambda \Upsilon_r, \qquad q_z = \lambda \Upsilon_z + \pi/2, \quad (25)$$

the radial and polar coordinates become 2π-periodic functions of (q_r, q_z), with Υ_r and Υ_z denoting the radial and polar frequencies in Mino time.

Explicit solutions can be written in terms of Jacobi elliptic functions [88]:

$$r(q_r) = \frac{r_3(r_1 - r_2)\mathrm{sn}^2(\frac{\mathrm{K}(k_r)}{\pi} q_r | k_r) - r_2(r_1 - r_3)}{(r_1 - r_2)\mathrm{sn}^2(\frac{\mathrm{K}(k_r)}{\pi} q_r | k_r) - (r_1 - r_3)}, \quad (26)$$

$$z(q_z) = z_1 \mathrm{sn}\left(\mathrm{K}(k_z)\frac{2q_z}{\pi}\middle| k_z\right), \quad (27)$$

where $\mathrm{K}(k)$ is the complete elliptic integral of the first kind and $\mathrm{sn}(u|k)$ the Jacobi elliptic sine. Their definitions and conventions are summarized in Appendix A.

The additional roots r_3, r_4 and constant z_2 relate to r_1, r_2, z_1 as

$$r_3 = \frac{1}{1-\mathcal{E}^2} - \frac{r_1 + r_2}{2} + \sqrt{\left(\frac{r_1 + r_2}{2} - \frac{1}{1-\mathcal{E}^2}\right)^2 - \frac{a^2\mathcal{Q}}{r_1 r_2 (1-\mathcal{E}^2)}}, \quad (28)$$

$$r_4 = \frac{a^2\mathcal{Q}}{r_1 r_2 r_3 (1-\mathcal{E}^2)}, \quad (29)$$

$$z_2 = \sqrt{a^2(1-\mathcal{E}^2) + \frac{\mathcal{L}^2}{1 - z_1^2}}, \quad (30)$$

with elliptic moduli

$$k_r = \frac{(r_1 - r_2)(r_3 - r_4)}{(r_1 - r_3)(r_2 - r_4)}, \qquad k_z = a^2(1-\mathcal{E}^2)\frac{z_1^2}{z_2^2}. \quad (31)$$

From these solutions, the frequencies are

$$\Upsilon_r = \frac{\pi}{2\mathrm{K}(k_r)}\sqrt{(1-\mathcal{E}^2)(r_1 - r_3)(r_2 - r_4)}, \quad (32)$$

$$\Upsilon_z = \frac{\pi z_2}{2\mathrm{K}(k_z)}. \quad (33)$$

The geodesic equations for t and ϕ can be solved analogously. Equation (20) can be decomposed as

$$T(r, z) = T_t + T_r(r) + T_z(z), \quad (34)$$

where T_t is independent of r and z. Integrating $T(r, z)$ yields

$$t(\lambda) = \int \frac{T_r(r)}{\mathrm{d}r/\mathrm{d}\lambda}\mathrm{d}r + \int \frac{T_z(z)}{\mathrm{d}z/\mathrm{d}\lambda}\mathrm{d}z + T_t\lambda, \quad (35)$$

leading to the solution

$$t(q_t, q_r, q_z) = q_t + t_r(q_r) + t_z(q_z), \quad (36)$$

with t_r and t_z expressed in terms of elliptic integrals, as follows:

$$t_r(q_r) = \tilde{t}_r\left[\mathrm{am}\left(\mathrm{K}(k_r)\frac{q_r}{\pi}\middle| k_r\right)\right] - \frac{\tilde{t}_r(\pi)}{2\pi}q_r, \quad (37a)$$

$$t_z(q_z) = \tilde{t}_z\left[\mathrm{am}\left(\mathrm{K}(k_z)\frac{q_z}{\pi}\middle| k_z\right)\right] - \frac{\tilde{t}_z(\pi)}{2\pi}q_z, \quad (37b)$$

where am is the Jacobi amplitude function. Applying the same procedure to ϕ, we find

$$\phi(q_\phi, q_r, q_z) = q_\phi + \phi_r(q_r) + \phi_z(q_z), \quad (38)$$

where

$$\phi_r(q_r) = \tilde{\phi}_r\left[\mathrm{am}\left(\mathrm{K}(k_r)\frac{q_r}{\pi}\middle| k_r\right)\right] - \frac{\tilde{\phi}_r(\pi)}{2\pi}q_r, \quad (39a)$$

$$\phi_z(q_z) = \tilde{\phi}_z\left[\mathrm{am}\left(\mathrm{K}(k_z)\frac{q_z}{\pi}\middle| k_z\right)\right] - \frac{\tilde{\phi}_z(\pi)}{2\pi}q_z. \quad (39b)$$

[2]These quantities can be shifted by arbitrary initial phases. We choose $z(0) = z_1$, $z(\pi) = -z_1$, $r(0) = r_2$, and $r(\pi) = r_1$, allowing consistent integration over $q_r \in [0, \pi]$ in the computation of adiabatic fluxes.

The phases q_t and q_ϕ represent the secularly growing linear parts of the motion,

$$q_i = \Upsilon_i \lambda, \qquad \Upsilon_i = \tilde{\Upsilon}_{i,r} + \tilde{\Upsilon}_{i,z}, \qquad i = t, \phi, \tag{40}$$

where the functions $\tilde{t}_r, \tilde{t}_z, \tilde{\phi}_r, \tilde{\phi}_z, \tilde{\Upsilon}_{i,r}, \tilde{\Upsilon}_{i,z}$ are listed in Appendix B.

So far, we have discussed geodesic motion in terms of $\{\mathcal{E}, \mathcal{L}, \mathcal{Q}\}$. It is convenient to parametrize geodesics using orbital parameters p, e, and $\theta_{\rm inc}$, namely the semilatus rectum, the eccentricity, and the inclination angle measured with respect to the equatorial plane. In terms of these quantities, the radial and polar turning points r_1, r_2, and z_1 are

$$r_1 = \frac{p}{1-e}, \qquad r_2 = \frac{p}{1+e}, \qquad z_1 = \sin\theta_{\rm inc}. \tag{41}$$

Given the orbital elements r_1, r_2, and z_1, the constants of motion $\{\mathcal{E}, \mathcal{L}, \mathcal{Q}\}$ can be computed as

$$\mathcal{E} = \sqrt{\frac{\kappa\rho + 2\epsilon\sigma - 2a\sqrt{\frac{\sigma}{a^2}}(\sigma\epsilon^2 + \rho\epsilon\kappa - \eta\kappa^2)}{\rho^2 + 4\eta\sigma}}, \tag{42}$$

$$\mathcal{L} = -\frac{g(r_2)\mathcal{E}}{h(r_2)} - \frac{\sqrt{(g(r_2)^2 + h(r_2)f(r_2))\mathcal{E}^2 - h(r_2)d(r_2)}}{h(r_2)}, \tag{43}$$

$$\mathcal{Q} = z_1^2\left(a^2(1-\mathcal{E}^2) + \frac{\mathcal{L}^2}{1-z_1^2}\right), \tag{44}$$

where the auxiliary coefficients are defined as

$$\kappa = d(r_2)h(r_1) - d(r_1)h(r_2), \tag{45}$$

$$\epsilon = d(r_2)g(r_1) - d(r_1)g(r_2), \tag{46}$$

$$\rho = f(r_2)h(r_1) - f(r_1)h(r_2), \tag{47}$$

$$\eta = f(r_2)g(r_1) - f(r_1)g(r_2), \tag{48}$$

$$\sigma = g(r_2)h(r_1) - g(r_1)h(r_2), \tag{49}$$

and the functions $d(r)$, $f(r)$, $g(r)$, and $h(r)$ read

$$d(r) = \Delta(r)(r^2 + a^2 z_1^2), \tag{50}$$

$$f(r) = r^4 + a^2(r(r+2) + z_1^2\Delta(r)), \tag{51}$$

$$g(r) = 2ar, \tag{52}$$

$$h(r) = r(r-2) + \frac{z_1^2\Delta(r)}{1-z_1^2}. \tag{53}$$

C. Scalar field perturbations

Since the equations governing the metric perturbations coincide with those of GR, we focus here on the computation of scalar field perturbations sourced by the secondary charged BH orbiting the massive primary. We emphasize, however, that our numerical framework is fully capable of treating both scalar and tensor modes, as discussed in Sec. III.

The equation for $\psi^{(1)}$, Eq. (11), can be written explicitly in Boyer-Lindquist coordinates as [89]

$$\left[\frac{(r^2+a^2)^2}{\Delta} - a^2\sin^2\theta\right]\frac{\partial^2\psi^{(1)}}{\partial t^2} + \frac{4Mar}{\Delta}\frac{\partial^2\psi^{(1)}}{\partial t\partial\phi} + \left[\frac{a^2}{\Delta} - \frac{1}{\sin^2\theta}\right]\frac{\partial^2\psi^{(1)}}{\partial\phi^2} - \frac{\partial}{\partial r}\left[\Delta\frac{\partial\psi^{(1)}}{\partial r}\right] - \frac{1}{\sin\theta}\frac{\partial}{\partial\theta}\left[\sin\theta\frac{\partial\psi^{(1)}}{\partial\theta}\right] = -4\pi\Sigma T. \tag{54}$$

The scalar field $\psi^{(1)}(t, r, \theta, \phi)$ and the source term $T(t, r, \theta, \phi)$ admit expansions in spin-weighted spheroidal harmonics. In the frequency domain, after a Fourier transform, they read

$$\psi^{(1)}(x^\mu) = \int \mathrm{d}\omega \sum_{\ell m} \tilde{R}_{\ell m}(\omega, r) S_{\ell m}(\omega, \theta) e^{im\phi} e^{-i\omega t}, \tag{55}$$

$$J(x^\mu) = 4\pi\Sigma T(x^\mu) = \int \mathrm{d}\omega \sum_{\ell m} \tilde{J}_{\ell m}(\omega, r) S_{\ell m}(\omega, \theta) e^{im\phi} e^{-i\omega t}. \tag{56}$$

Here $\ell = 0, \ldots, \infty$ and $-\ell \le m \le \ell$. The decomposition (55)–(56) decouples the Teukolsky equation into angular and radial parts. The angular equation is

$$\left[\frac{1}{\sin\theta}\frac{\mathrm{d}}{\mathrm{d}\theta}\left(\sin\theta\frac{\mathrm{d}}{\mathrm{d}\theta}\right) - \gamma^2\sin^2\theta - \frac{m^2}{\sin^2\theta} + 2m\gamma + \lambda_{\ell m}\right] S_{\ell m} = 0, \tag{57}$$

where $\gamma = a\omega$, and $\lambda_{\ell m}$ is the angular eigenvalue. The solutions $S_{\ell m}(\omega, \theta)$ are spin-weighted spheroidal harmonics, satisfying the orthogonality relation

$$\int \mathrm{d}\Omega S_{\ell m}(\omega, \theta) e^{im\phi} S^*_{\ell' m'}(\omega, \theta) e^{-im'\phi} = \delta_{\ell\ell'}\delta_{mm'}. \tag{58}$$

The radial functions $\tilde{R}_{\ell m}(\omega, r)$ satisfy the inhomogeneous equation

$$\frac{\mathrm{d}}{\mathrm{d}r}\left[\Delta\frac{\mathrm{d}\tilde{R}_{\ell m}}{\mathrm{d}r}\right]+\left[\frac{K^2}{\Delta}-\lambda_{\ell m}\right]\tilde{R}_{\ell m}=\tilde{J}_{\ell m}, \tag{59}$$

where $K(\omega,r)=(r^2+a^2)\omega-am$. The solution to Eq. (59) can be found with the standard Green's function method:

$$\tilde{R}_{\ell m}=\tilde{R}^{+}_{\ell m}\int_{r_+}^{r}\mathrm{d}r'\,\frac{\tilde{R}^{-}_{\ell m}\tilde{J}_{\ell m}}{W_{\ell m}\Delta}+\tilde{R}^{-}_{\ell m}\int_{r}^{\infty}\mathrm{d}r'\,\frac{\tilde{R}^{+}_{\ell m}\tilde{J}_{\ell m}}{W_{\ell m}\Delta}, \tag{60}$$

where $\tilde{R}^{-}_{\ell m}$ ($\tilde{R}^{+}_{\ell m}$) denote the purely ingoing (outgoing) solution at the horizon (infinity) of the homogeneous equation and the Wronskian is

$$W_{\ell m}=\frac{\mathrm{d}\tilde{R}^{+}_{\ell m}}{\mathrm{d}r}\tilde{R}^{-}_{\ell m}-\tilde{R}^{+}_{\ell m}\frac{\mathrm{d}\tilde{R}^{-}_{\ell m}}{\mathrm{d}r}. \tag{61}$$

The asymptotic behavior of the solutions $\tilde{R}^{\pm}_{\ell m}$ are easier to find if we introduce the auxiliary functions:

$$\tilde{Y}^{\pm}_{\ell m}(\omega,r)=\sqrt{r^2+a^2}\tilde{R}^{\pm}_{\ell m}(\omega,r), \tag{62}$$

which satisfies the homogeneous equation

$$\frac{\mathrm{d}^2}{\mathrm{d}r_\star^2}\tilde{Y}^{\pm}_{\ell m}+V\tilde{Y}^{\pm}_{\ell m}=0, \tag{63}$$

where $r_\star$ is the tortoise coordinate defined by

$$\frac{\mathrm{d}r_\star}{\mathrm{d}r}=\frac{r^2+a^2}{\Delta}, \tag{64}$$

and the effective potential is

$$V(\omega,r)=\frac{K(\omega,r)^2-\lambda_{\ell m}\Delta(r)}{(r^2+a^2)^2}-G(r)^2-\frac{\mathrm{d}G(r)}{\mathrm{d}r_\star}, \tag{65}$$

with $G=\frac{r\Delta}{(r^2+a^2)^2}$.

At spatial infinity ($r\to\infty$, $r_\star\to\infty$) and near the horizon ($r\to r_+$, $r_\star\to-\infty$), Eq. (63) reduces to

$$\frac{\mathrm{d}^2}{\mathrm{d}r_\star^2}\tilde{Y}^{\pm}_{\ell m}+\omega^2\tilde{Y}^{\pm}_{\ell m}=0 \qquad (r_\star\to+\infty), \tag{66a}$$

$$\frac{\mathrm{d}^2}{\mathrm{d}r_\star^2}\tilde{Y}^{\pm}_{\ell m}+k^2\tilde{Y}^{\pm}_{\ell m}=0 \qquad (r_\star\to-\infty), \tag{66b}$$

where $k=\omega-m\omega_+$ and $\omega_+=a/(2Mr_+)$.

From Eq. (66), we find the asymptotic behavior of the functions $\tilde{Y}^{\pm}_{\ell m}$, i.e., $\tilde{Y}^{-}_{\ell m}\sim e^{-ikr_\star}$ for $r\to-\infty$ and $\tilde{Y}^{+}_{\ell m}\sim e^{+i\omega r_\star}$ for $r\to+\infty$. From these, using Eq. (62), we find the asymptotic behavior of the functions $\tilde{R}^{\pm}_{\ell m}$. We choose their normalizations such that

$$\tilde{R}^{-}_{\ell m}\to e^{-ikr_\star} \qquad (r_\star\to-\infty), \tag{67a}$$

$$\tilde{R}^{-}_{\ell m}\to A^{\mathrm{in}}_{\ell m}\frac{e^{-i\omega r_\star}}{r}+A^{\mathrm{out}}_{\ell m}\frac{e^{i\omega r_\star}}{r} \qquad (r_\star\to+\infty), \tag{67b}$$

and

$$\tilde{R}^{+}_{\ell m}\to B^{\mathrm{in}}_{\ell m}e^{-ikr_\star}+B^{\mathrm{out}}_{\ell m}e^{ikr_\star} \qquad (r_\star\to-\infty), \tag{68a}$$

$$\tilde{R}^{+}_{\ell m}\to\frac{e^{i\omega r_\star}}{r} \qquad (r_\star\to+\infty). \tag{68b}$$

The radial solution $\tilde{R}_{\ell m}$ in Eq. (60) is ingoing (outgoing) at the horizon (infinity) by construction and its asymptotic amplitude $\delta\tilde{\psi}^{-}_{\ell m}$ ($\delta\tilde{\psi}^{+}_{\ell m}$), i.e.,

$$\delta\tilde{\psi}^{\mp}_{\ell m}(\omega)=\int_{r_+}^{+\infty}\mathrm{d}r\,\frac{\tilde{R}^{\pm}_{\ell m}(\omega,r)\tilde{J}_{\ell m}(\omega,r)}{W_{\ell m}(\omega,r)\Delta(r)}, \tag{69}$$

is the physical relevant quantity for computing GW fluxes. In Eq. (69), the product $W\Delta$ is independent of r; evaluating it as $r\to\infty$ gives

$$w_{\ell m}(\omega)=W_{\ell m}(\omega,r)\Delta(r)|_{r\to\infty}=2i\omega A^{\mathrm{in}}_{\ell m}(\omega). \tag{70}$$

D. The source term

We now turn our attention on the frequency-domain components, $\tilde{J}_{\ell m}(\omega,r)$, that appear as source terms of the scalar field equation (59),

$$\tilde{J}_{\ell m}(\omega,r)=\frac{1}{2\pi}\int_{-\infty}^{+\infty}\mathrm{d}t\int\sin\theta\,\mathrm{d}\theta\,\mathrm{d}\phi\,S_{\ell m}(\omega,\theta)\times e^{i\omega t-im\phi}J(t,r,\theta,\phi), \tag{71}$$

where the time-domain source reads [see Eq. (11)]

$$J=4\pi m_{\mathrm{p}}d\frac{\delta(r-r_{\mathrm{p}})\delta(\theta-\theta_{\mathrm{p}})\delta(\phi-\phi_{\mathrm{p}})}{|\sin\theta|\dot{t}}, \tag{72}$$

with $\dot{t}=\mathrm{d}t/\mathrm{d}\tau$. The functions r_{p}, θ_{p}, and ϕ_{p} denote the coordinates of the secondary, and depend on the coordinate time, e.g., $r_{\mathrm{p}}=r_{\mathrm{p}}(t)$. Swapping the order of the time and spatial integrals, replacing Eq. (72) into Eq. (71), and performing the angular integrals, we get

$$\tilde{J}_{\ell m}=2m_{\mathrm{p}}d\int_{-\infty}^{+\infty}\frac{\mathrm{d}t}{\dot{t}}S_{\ell m}e^{i(\omega t-m\phi)}\delta(r-r_{\mathrm{p}})\Big|_{\substack{\phi=\phi_{\mathrm{p}}\\ \theta=\theta_{\mathrm{p}}}}, \tag{73}$$

where we used $|\sin(\theta)|=\sin\theta$ since $\theta\in[0,\pi]$.

Plugging Eq. (73) in Eq. (69) and performing the integration over r, we get the explicit expression of the mode amplitudes $\delta\tilde{\varphi}^{\pm}_{\ell m}$, as follows:

$$\delta\tilde{\psi}^{\mp}_{\ell m} = \frac{2m_{\rm p}d}{w_{\ell m}} \int_{-\infty}^{+\infty} \frac{{\rm d}t}{\dot{t}}\, e^{i(\omega t - m\phi)} \tilde{R}^{\pm}_{\ell m} S_{\ell m}\Big|_{\substack{\phi=\phi_{\rm p} \\ \theta=\theta_p \\ r=r_{\rm p}}}. \quad (74)$$

Writing the t and ϕ particles' coordinates in terms of the Mino time λ, we obtain

$$\begin{aligned} t(\lambda) &= \Upsilon_t \lambda + t_r(r(\lambda)) + t_\theta(\theta(\lambda)), \\ \phi(\lambda) &= \Upsilon_\phi \lambda + \phi_r(r(\lambda)) + \phi_\theta(\theta(\lambda)), \end{aligned} \quad (75)$$

where Υ_i are the Mino frequencies; the mode coefficients read

$$\delta\tilde{\psi}^{\mp}_{\ell m} = \frac{2m_{\rm p}d}{w_{\ell m}} \int_{-\infty}^{+\infty} {\rm d}\lambda e^{i(\omega\Upsilon_t - m\Upsilon_\phi)\lambda} \mathcal{I}^{\pm}_{\ell m}, \quad (76)$$

with

$$\begin{aligned} \mathcal{I}^{\pm}_{\ell m}(\omega, r(\lambda), \theta(\lambda)) = e^{i[\omega(t_r(r)+t_\theta(\theta)) - m(\phi_r(r)+\phi_\theta(\theta))]} \\ \times \Sigma(r,\theta)\tilde{R}^{\pm}_{\ell m}(\omega, r) S_{\ell m}(\omega,\theta)\Big|_{\substack{r=r_{\rm p}(\lambda) \\ \theta=\theta_{\rm p}(\lambda)}}. \end{aligned} \quad (77)$$

Since $\mathcal{I}^{\pm}$ is a periodic function of λ, it admits a Fourier expansion

$$\mathcal{I}^{\pm}_{\ell m} = \sum_{kn} \hat{\mathcal{I}}^{\pm}_{\ell mkn} e^{-i(k\Upsilon_\theta + n\Upsilon_r)\lambda}, \quad (78)$$

where k and n are the angular and radial harmonic index respectively, with coefficients

$$\begin{aligned} \hat{\mathcal{I}}^{\pm}_{\ell mkn}(\omega) = \frac{1}{(2\pi)^2} \int_0^{2\pi} {\rm d}q_\theta \int_0^{2\pi} {\rm d}q_r e^{i(kq_\theta + nq_r)} \\ \times \mathcal{I}^{\pm}_{\ell m}[\omega, r(q_r), \theta(q_\theta)], \end{aligned} \quad (79)$$

where we used the angle variables q_r and q_θ defined in Eq. (25). Inserting Eq. (77) into Eq. (76), we obtain:

$$\delta\tilde{\psi}^{\pm}_{\ell m}(\omega) = \sum_{kn} \delta\hat{\psi}^{\pm}_{\ell mkn} \delta(\omega - \omega_{mkn}), \quad (80)$$

with

$$\omega_{mkn} = k\Omega_\theta + n\Omega_r + m\Omega_\phi, \qquad \Omega_i = \frac{\Upsilon_i}{\Upsilon_t}, \quad (81)$$

and

$$\begin{aligned} \delta\hat{\psi}^{\mp}_{\ell mkn} = \frac{m_{\rm p}d}{\pi w \Upsilon_t} \int_0^{2\pi} {\rm d}q_\theta \int_0^{2\pi} {\rm d}q_r e^{i(kq_\theta + nq_r)} \\ \times \mathcal{I}^{\pm}_{\ell m}(\omega_{mkn}, r(q_r), \theta(q_\theta)). \end{aligned} \quad (82)$$

Noting that (with $i = r, \theta$), we obtain

$$\begin{aligned} r(q_i) &= r(-q_i), \\ t_i(q_i) &= -t_i(-q_i), \\ \phi_i(q_i) &= -\phi_i(-q_i), \end{aligned} \quad (83)$$

we can further simplify the domain of integration. Indeed, applying these symmetries to the integrand in Eq. (82), the amplitudes of the radial Teukolsky function become

$$\begin{aligned} \delta\hat{\psi}^{\mp}_{\ell mkn} &= \frac{4m_{\rm p}d}{w\pi\Upsilon_t} \int_0^{\pi} {\rm d}q_\theta \int_0^{\pi} {\rm d}q_r \Sigma \tilde{R}^{\pm}_{\ell m}(\omega, r_{\rm p}(q_r)) S_{\ell m}(\theta_{\rm p}(q_\theta), \omega) \cos[nq_r + \omega t_r(q_r) - m\phi_r(q_r)] \cos[nq_\theta + \omega t_\theta(q_\theta) - m\phi_\theta(q_\theta)] \\ &= \frac{4m_{\rm p}d}{w\pi\Upsilon_t} (I^{(1)}_\theta I^{\pm(2)}_r + I^{(2)}_\theta I^{\pm(1)}_r), \end{aligned} \quad (84)$$

where

$$\begin{aligned} I^{(1)}_\theta &= \int_0^{\pi} {\rm d}q_\theta\, S_{\ell m}(\theta_{\rm p}(q_\theta), \omega) \cos[kq_\theta + \omega t_\theta(q_\theta) - m\phi_\theta(q_\theta)], \\ I^{(2)}_\theta &= \int_0^{\pi} {\rm d}q_\theta\, a^2 \cos^2(\theta_{\rm p}(q_\theta)) S_{\ell m}(\theta_{\rm p}(q_\theta), \omega) \cos[kq_\theta + \omega t_\theta(q_\theta) - m\phi_\theta(q_\theta)], \\ I^{\pm(1)}_r &= \int_0^{\pi} {\rm d}q_r\, \tilde{R}^{\pm}_{\ell m}(\omega, r_{\rm p}(q_r)) \cos[nq_r + \omega t_r(q_r) - m\phi_r(q_r)], \\ I^{\pm(2)}_r &= \int_0^{\pi} {\rm d}q_r\, r_p^2(q_r) \tilde{R}^{\pm}_{\ell m}(\omega, r_{\rm p}(q_r)) \cos[nq_r + \omega t_r(q_r) - m\phi_r(q_r)]. \end{aligned} \quad (85)$$

E. Energy and angular momentum scalar fluxes

The energy and angular momentum fluxes associated to the scalar field perturbation, carried away at the horizon (−) and at infinity (+), can be computed as

$$\dot{E}^{\pm} = \mp\Delta \int T^{\rm scal}_{tr} \mathrm{d}\Omega, \qquad \dot{L}^{\pm} = \mp\Delta \int T^{\rm scal}_{\phi r} \mathrm{d}\Omega, \quad (86)$$

where the components of the stress-energy tensor needed to determine $\dot{E}^{\pm}$ and $\dot{L}^{\pm}$ are

$$T^{\rm scal}_{jr} = \frac{1}{16\pi}\partial_j\psi\partial_r\psi = \frac{1}{16\pi}\partial_j\psi(\partial_r\psi)^*, \quad j=\{t,\phi\}, \quad (87)$$

since the scalar field is real. From the spheroidal harmonics expansion (55), and the asymptotic behavior of the radial function $\tilde{R}_{\ell m}(\omega, r)$ at the horizon and at spatial infinity, Eqs. (67) and (68), we find

$$\begin{aligned} \psi_{\ell m} &\sim e^{-i\omega t}e^{-ikr_\star}S_{\ell m}e^{im\phi} && r\to r_+ \\ \psi_{\ell m} &\sim e^{-i\omega t}\frac{e^{i\omega r_\star}}{r}S_{\ell m}e^{im\phi} && r\to+\infty. \end{aligned} \quad (88)$$

From this, we find the t and ϕ derivatives of the scalar field in both limits $r\to r_+$, $r\to+\infty$, as follows:

$$\partial_t\psi = -i\omega\psi, \qquad \partial_\phi\psi = im\psi, \quad (89)$$

while the derivative respect to the radial coordinate shows different asymptotic behaviors, as follows:

$$\begin{aligned} (\partial_r\psi)^* &\sim e^{i\omega t}\frac{r^2+a^2}{\Delta}(-ik)e^{ikr_\star}S_{\ell m}e^{-im\phi} && r\to r_+, \\ (\partial_r\psi)^* &\sim e^{i\omega t}(-i\omega)\frac{e^{-i\omega r_\star}}{r}S_{\ell m}e^{-im\phi} && r\to+\infty. \end{aligned} \quad (90)$$

Using the orthogonality properties of the spheroidal harmonics, Eq. (58), we obtain the final expressions for the energy fluxes at infinity and at the horizon[3]:

$$\begin{aligned} \dot{E}^{+} &= \sum_{\ell mnk}\dot{E}^{+}_{\ell mnk} \\ &= \frac{1}{16\pi}\sum_{\ell mnk}\omega^2_{mnk}|\delta\psi^{+}_{\ell mnk}|^2, \\ \dot{E}^{-} &= \sum_{\ell mnk}\dot{E}^{-}_{\ell mnk} \\ &= \frac{1}{16\pi}\sum_{\ell mnk}\omega_{mnk}k_{mnk}|\delta\psi^{-}_{\ell mnk}|^2(r_+^2+a^2), \end{aligned} \quad (91)$$

and for the angular momentum fluxes at infinity and at horizon:

$$\begin{aligned} \dot{L}^{+} &= \sum_{\ell mnk}\dot{L}^{+}_{\ell mnk} \\ &= \frac{1}{16\pi}\sum_{\ell mnk}m\omega_{mnk}|\delta\psi^{+}_{\ell mnk}|^2, \\ \dot{L}^{-} &= \sum_{\ell mnk}\dot{L}^{-}_{\ell mnk} \\ &= \frac{1}{16\pi}\sum_{\ell mnk}mk_{mnk}|\delta\psi^{-}_{\ell mnk}|^2(r_+^2+a^2), \end{aligned} \quad (92)$$

with $k_{mnk} = \omega_{mnk} - m\omega_+$. Note that since each flux mode satisfies $\dot{L}^{\pm}_{\ell mnk} = (m/\omega_{mnk})\dot{E}^{\pm}_{\ell mnk}$, the angular momentum fluxes can be straightforwardly obtained from the energy fluxes (and vice versa). The same applies to the rate of change of the Carter constant, which can be obtained from the energy and angular momentum fluxes [46,90,91].

In Eqs. (91) and (92), we have neglected possible couplings among different (n,k) modes. Indeed, some harmonics can give rise to *resonances* [92]: their averaged crossing term is not vanishing and it contributes to the energy and angular momentum fluxes. It occurs if

$$\exists\, k,n\in\mathbb{Z}:\ k\Omega_\phi + n\Omega_\theta = 0. \quad (93)$$

Resonances contribute at order $\epsilon^{-1/2}$ in the waveform frequency, and they can be consistently neglected at leading order ϵ [93]. In this regard, a resonant scalar self-force model was presented in Ref. [94].

III. RESULTS

To compute scalar fluxes we use STORM, a new C++ framework designed to model the evolution of asymmetric binaries in generic extensions of GR [59]. The code supports arbitrary-precision arithmetic through the `Boost` multiprecision library [95], and implements all numerical ingredients required to evaluate perturbations of spinning BHs. Its structure is organized into seven main modules:

(i) `SpinWeightedSpheroidalHarmonics` evaluates the homogeneous solutions of the angular Teukolsky equation for arbitrary spin weight s, providing the angular basis functions used in the mode decomposition;
(ii) `RadialHomogeneousSolution` computes the solutions of the homogeneous radial Teukolsky equation for arbitrary field spin s, which are required to construct the radial Green's function;
(iii) `GeodesicOrbitalMotion` integrates the geodesic motion of the secondary along eccentric and inclined Kerr orbits (see Sec. II B), supplying the source trajectories for the perturbation equations;

[3]Notice that the expression for the horizon flux differs from that in Ref. [53] due to a different normalization of the ingoing solution for the homogeneous equation that was adopted there.

(iv) `ScalarFluxMode` evaluates the energy flux of individual scalar modes [c.f., Eq. (91)];
(v) `GravitationalFluxMode` evaluates the energy flux of individual gravitational modes;
(vi) `special_functions` provides high-accuracy implementations of complex special functions, including the Γ function and hypergeometric functions, which appear in the analytic solutions of the Teukolsky equations; and
(vii) `config`: a configuration file which allows the user to select the numerical data type (e.g., double or multiprecision) and to set the tolerance parameters controlling all iterative procedures. In this way, the user can balance computational cost and numerical accuracy according to the requirements of the specific application.

A detailed description of the numerical methods used to solve the angular and radial Teukolsky equations is provided in Appendix C.

With this computational infrastructure in hand, we carry out a systematic exploration of the scalar radiation emitted by generic binaries, mapping out the full four-index mode structure (ℓ, m, n, k) associated with general trajectories, both inclined and eccentric.

Spectra of the scalar fluxes shown hereafter are generated by fixing the orbital parameters $(a, e, p, \theta_{\rm inc})$ and the angular mode numbers (ℓ, m), while performing a systematic scan in the (k, n) harmonic plane.

For a given value of k, the Fourier index n is first set to $n = 0$ and then scanned toward both positive and negative values. All mode contributions to the energy flux with $|\dot{E}^{\pm}_{\ell mkn}| < \bar{\dot{E}}^{\pm}_{\ell mkn} = 10^{-30}$ are set to zero. Here we take the absolute value, since $\dot{E}^{-}_{\ell mkn}$ can take negative values. The scan in a given direction is terminated once three consecutive values of n yield vanishing contributions. This procedure is repeated for successive values of k, starting from $k = 0$ and scanning toward both positive and negative k. In each direction, the scan over k is stopped when the sum over n of the corresponding modes falls below the numerical threshold, $\sum_n \dot{E}^{\pm}_{\ell mkn} < \bar{\dot{E}}^{\pm}_{\ell mkn}$, for three consecutive values of k. The scan over k can be simplified by observing that, for a fixed value of $\ell + m$, only k-modes with matching parity contribute. Specifically, when $\ell + m$ is even (odd), only even (odd) values of k appear in the sum. This selection rule follows from the parity properties of the angular functions and is discussed in Appendix B of Ref. [45] for the case of inclined, circular orbits. We apply the same criterion to fluxes of angular momentum, finding that the sum over n and k saturates the threshold at the same values as for the energy fluxes (see Tables III–IV and discussion below).

Figure 1 shows a representative example of the scalar energy and angular momentum fluxes at the horizon and at infinity for a binary configuration with $(a/M, e, p/M, \theta_{\rm inc}) = (0.5, 0.2, 25, 5°)$. Each panel displays a two-dimensional

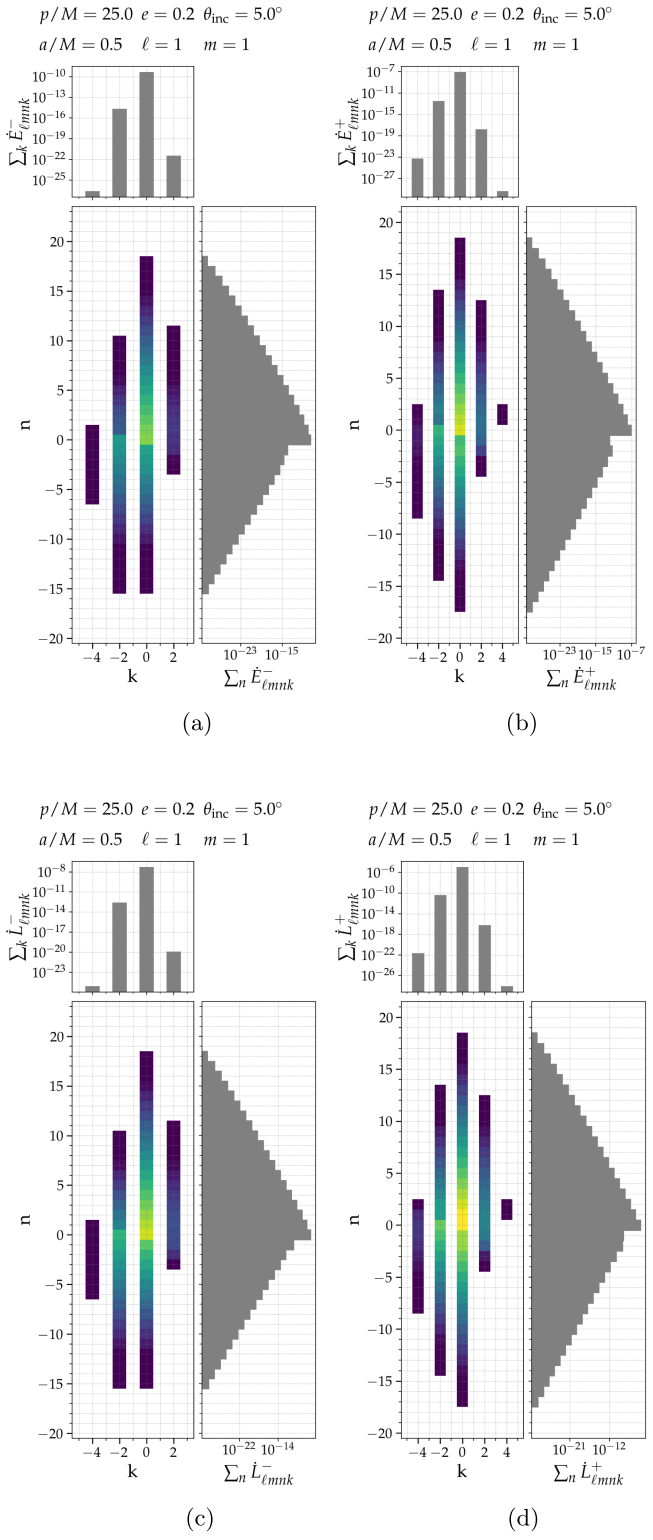


FIG. 1. Spectrum of the scalar energy (top panels) and angular momentum (bottom panels) fluxes emitted at the horizon (left panels) and at infinity (right panels) for the $(\ell, m) = (1, 1)$ harmonic, corresponding to a binary configuration with $(a/M, e, p/M, \theta_{\rm inc}) = (0.5, 0.2, 25, 5°)$. The central panel in each plot shows the mode contributions in the (n, k) plane, with the color scale indicating the magnitude of the single-mode flux. The top (right) panels display the *marginalized* energy flux contributions, obtained for a given k (n) by summing over the index n (k). (a) Energy scalar flux at the horizon, (b) energy scalar flux at infinity, (c) angular momentum scalar flux at horizon, and (d) angular momentum scalar flux at infinity.

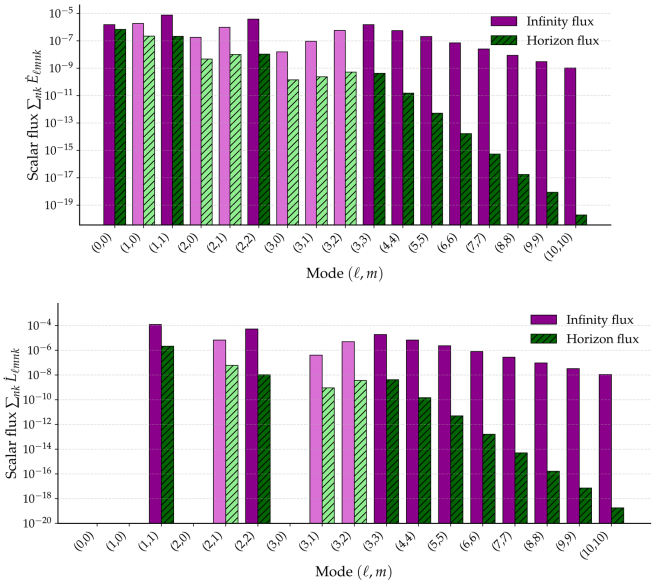


FIG. 2. Bar plot of the energy (top panel) and angular momentum (bottom panel) fluxes at infinity and at the horizon, for scalar modes with different angular indices (ℓ, m), summed over the (n, k) harmonics. Darker (lighter) shades denote modes with $\ell = m$ ($\ell \neq m$), respectively.

distribution of mode contributions in the (n, k) plane, together with the corresponding marginal distributions, which are constructed by summing the computed mode contributions over n or k, respectively. Finally, the color scale indicates the magnitude of the single-mode flux.

A. Mode hierarchy across ℓ and m

We begin by analyzing the dependence of the scalar flux on the harmonic indices (ℓ, m). To this end, we fix the orbital configuration to $(a/M, e, p/M, \theta_{\rm inc}) = (0.3, 0.5, 7, 30°)$, and have verified that the qualitative features described below persist across different setups.

Figure 2 presents bar plots of the energy and angular momentum fluxes, summed over the harmonic indices n and k, for selected (ℓ, m) modes. The corresponding numerical values are listed in Tables I–II. Representative spectra for these modes are shown in Figs. 9, 10, 15, and 16 of Appendix D.

The fluxes for (ℓ, m) and $(\ell, -m)$ are identical, as a consequence of the invariance under the transformation [96]

$$(\ell, m, n, k) \longrightarrow (\ell, -m, -n, -k), \tag{94}$$

which ensures symmetry under $m \to -m$ after summation over n and k. Accordingly, Table I includes only modes with $m \geq 0$.

The total flux decreases with increasing multipole order ℓ, with the dominant contribution arising from $\ell = 1$.

TABLE I. Scalar energy flux at infinity and at the horizon summed over n and k for different (ℓ, m) modes. Orbital parameters are fixed to $a/M = 0.3$, $e = 0.5$, $p/M = 7$, and $\theta_{\rm inc} = 30°$.

(ℓ, m)	$\sum_{n,k} \dot{E}^{+}_{\ell mnk}$	$\sum_{n,k} \dot{E}^{-}_{\ell mnk}$
(0, 0)	1.519×10^{-6}	6.829×10^{-7}
(1, 0)	1.851×10^{-6}	2.236×10^{-7}
(1, 1)	7.682×10^{-6}	2.119×10^{-7}
(2, 0)	1.810×10^{-7}	4.789×10^{-9}
(2, 1)	9.658×10^{-7}	9.943×10^{-9}
(2, 2)	3.836×10^{-6}	1.071×10^{-8}
(3, 0)	1.572×10^{-8}	1.418×10^{-10}
(3, 1)	9.291×10^{-8}	2.363×10^{-10}
(3, 2)	5.832×10^{-7}	5.216×10^{-10}
(3, 3)	1.531×10^{-6}	4.312×10^{-10}
(4, 4)	5.689×10^{-7}	1.543×10^{-11}
(5, 5)	2.045×10^{-7}	5.195×10^{-13}
(6, 6)	7.218×10^{-8}	1.695×10^{-14}
(7, 7)	2.518×10^{-8}	5.444×10^{-16}
(8, 8)	8.720×10^{-9}	1.739×10^{-17}
(9, 9)	3.027×10^{-9}	8.686×10^{-19}
(10, 10)	1.031×10^{-9}	1.938×10^{-20}

Modes with $m = 0$ do not carry angular momentum, and therefore satisfy $\dot{L}^{\pm}_{\ell mnk} = 0$.

Consistent with the behavior observed for eccentric orbits in Ref. [43], we find that for dominant modes with $\ell = m$ the location of the spectral peak depends strongly on ℓ. The peak in the k spectrum occurs at $k = 0$, while the

TABLE II. Scalar angular momentum flux at infinity and at the horizon summed over n and k for different (ℓ, m) modes. Orbital parameters are fixed to $a/M = 0.3$, $e = 0.5$, $p/M = 7$, and $\theta_{\rm inc} = 30°$.

(ℓ, m)	$\sum_{n,k} \dot{L}^{+}_{\ell mnk}$	$\sum_{n,k} \dot{L}^{-}_{\ell mnk}$
(0, 0)	0	0
(1, 0)	0	0
(1, 1)	1.237×10^{-4}	2.201×10^{-6}
(2, 0)	0	0
(2, 1)	6.793×10^{-6}	6.014×10^{-8}
(2, 2)	5.205×10^{-5}	1.059×10^{-8}
(3, 0)	0	0
(3, 1)	4.019×10^{-7}	9.244×10^{-10}
(3, 2)	4.926×10^{-6}	3.616×10^{-9}
(3, 3)	1.895×10^{-5}	4.149×10^{-9}
(4, 4)	6.688×10^{-6}	1.468×10^{-10}
(5, 5)	2.330×10^{-6}	4.905×10^{-12}
(6, 6)	8.055×10^{-7}	1.591×10^{-13}
(7, 7)	2.770×10^{-7}	5.091×10^{-15}
(8, 8)	9.487×10^{-8}	1.621×10^{-16}
(9, 9)	3.255×10^{-8}	7.222×10^{-18}
(10, 10)	1.105×10^{-8}	1.762×10^{-19}

TABLE III. Location of the maximum in the n spectrum for dominant modes with $\ell = m$ at $k = 0$, for fluxes of energy at infinity ($n^{+}_{\rm peak}$) and at horizon ($n^{-}_{\rm peak}$). Values in parentheses correspond to the location of maxima for the fluxes of angular momentum. We assume a binary system with $a/M = 0.3$, $e = 0.5$, $p/M = 7$, and $\theta_{\rm inc} = 30°$.

$\ell = m$	$n^{+}_{\rm peak}$	$n^{-}_{\rm peak}$
0	1	1
1	1(1)	4(3)
2	4(4)	6(6)
3	6(6)	10(9)
4	9(9)	13(12)
5	12(12)	16(16)
6	15(14)	19(19)
7	17(17)	22(22)
8	20(20)	26(25)
9	23(23)	49(49)
10	26(25)	32(32)

peak in the n spectrum shifts toward higher values as ℓ increases. For clarity, we define $n^{\pm}_{\rm peak}$ and $k^{\pm}_{\rm peak}$ as the harmonic indices at which $\dot{E}^{\pm}_{\ell mnk}$ (and equivalently $\dot{L}^{\pm}_{\ell mnk}$) attain their maximum values. Table III lists the harmonic index n corresponding to the maximum flux for $\ell = m = 0, 1, \ldots, 10$, at both infinity and the horizon.

For subdominant modes with $\ell \neq m$, the spectral structure is more intricate. Table IV summarizes the peak locations of $\dot{E}^{\pm}_{\ell mnk}$ and $\dot{L}^{\pm}_{\ell mnk}$. The maximum along n is primarily determined by ℓ and depends only weakly on m, whereas the peak along k is controlled by m. For all (ℓ, m) pairs analyzed, the maximum in k occurs at $k = \ell - m$, providing a practical guideline for selecting the initial k range when constructing scalar-flux grids for waveform generation.

Finally, the values of $n^{\pm}_{\rm peak}$ are nearly identical for the energy and angular momentum fluxes, for both $\ell = m$ and $\ell \neq m$, across all configurations analyzed.

TABLE IV. Peak locations $(k^{\pm}_{\rm peak}, n^{\pm}_{\rm peak})$ of modes with $\ell \neq m$ for fluxes of energy at infinity and at the horizon. Values in parentheses refer to peaks for fluxes of angular momentum. Binary parameters are fixed to $a/M = 0.3$, $e = 0.5$, $p/M = 7$, and $\theta_{\rm inc} = 30°$.

		Infinity flux		Horizon flux	
ℓ	m	$k^{+}_{\rm peak}$	$n^{+}_{\rm peak}$	$k^{-}_{\rm peak}$	$n^{-}_{\rm peak}$
1	0	1	1	1	3
2	0	2	3	2	5
2	1	1(1)	4(3)	1(1)	6(5)
3	0	3	6	3	8
3	1	2(2)	6(6)	2(2)	9(8)
3	2	1(1)	6(6)	1(1)	9(9)

B. Systematic exploration of the orbital-parameter dependence

As we have verified that the radiation is predominantly dipolar, we begin by constructing two-dimensional mode grids in the (n, k) plane for the $(\ell, m) = (1, 1)$ harmonic across a representative set of orbital configurations. We extract the scalar spectra for all possible combinations of the following orbital parameters:

$$a/M = \{0.1, 0.5, 0.9\}, \qquad e = \{0.2, 0.4, 0.8\},$$
$$\theta_{\rm inc} = \{5°, 40°, 85°\}, \qquad p/M = \{8, 25\}. \tag{95}$$

For illustrative purposes, we present in the main text figures corresponding to a subset of these configurations, focusing in particular on the impact of variations in inclination and eccentricity on the resulting flux spectra. The trends discussed below are observed throughout the entire parameter space explored (see Appendix D). The behavior of the energy and angular momentum spectra is also remarkably similar (cf., top and bottom rows of Fig. 1). For this reason, hereafter we only discuss the dependence of $\dot{E}$ on the binary parameters:

(i) Inclination angle. By comparing Figs. 1 and 3, we observe that increasing the inclination angle $\theta_{\rm inc}$ leads to a broadening of the distribution in the k direction, reflecting the richer harmonic structure of strongly inclined orbits. Despite this broadening, the

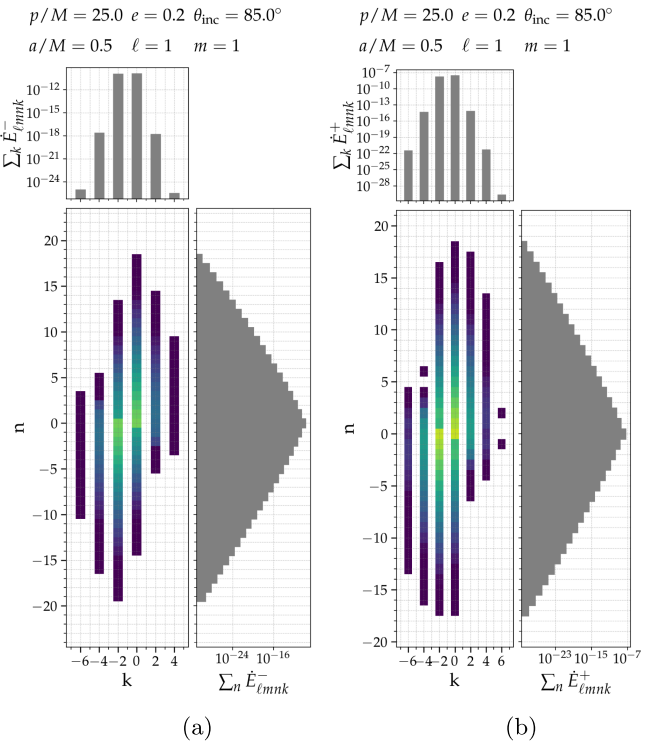


FIG. 3. Same as Figs. 1(a) and 1(b), but for $\theta_{\rm inc} = 85°$. (a) Energy scalar flux at the horizon and (b) energy scalar flux at infinity.

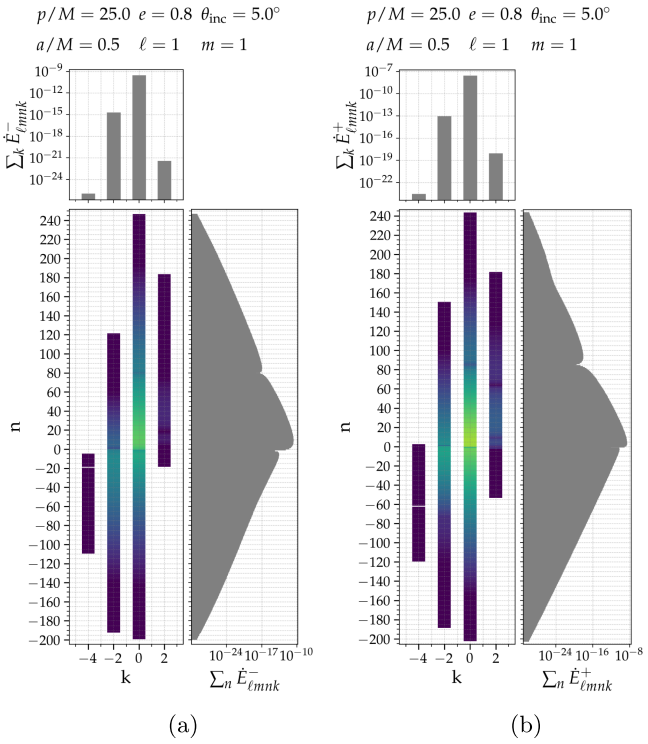


FIG. 4. Same as Figs. 1(a) and 1(b), but for $e = 0.8$. (a) Energy scalar flux at the horizon and (b) energy scalar flux at infinity.

flux remains strongly peaked at $k = 0$, with only a narrow range of k modes contributing significantly.

(ii) Eccentricity. Increasing the eccentricity e substantially broadens the spectrum along the n direction (see Fig. 4). For low eccentricity, the dominant contribution arises from the $n = 0$ mode, whereas at high eccentricity the peak shifts to $|n| \neq 0$, often accompanied by secondary maxima. This behavior becomes increasingly pronounced in relativistically strong-field configurations, namely for smaller orbital separations or highly inclined orbits.

(iii) Orbital radius. For larger values of p, the total flux summed over (n, k) decreases, as expected for orbits located further from the primary BH. This trend is quantified in Table V, which reports the total fluxes $\dot{E}^{\pm}$ for all configurations analyzed.

As discussed in previous studies [43,45], the structure of the scalar flux spectra becomes progressively richer as the complexity of the orbital motion increases. Overall, the simultaneous presence of orbital inclination and eccentricity does not qualitatively alter the main spectral features reported in the literature for eccentric equatorial orbits and circular inclined orbits.

For instance, at $a/M = 0.5$, the dominant harmonic in k is $k = 0$ for all values of n when $\theta_{\rm inc} = 5°$ and 40°.

TABLE V. Values of the scalar flux at infinity (horizon) summed over the n and k harmonics for the $(\ell, m) = (1, 1)$ mode. For each spin, we consider different values of the binary semilatus rectum p/M, inclination $\theta_{\rm inc}$, and eccentricity e.

p/M	$\theta_{\rm inc}$	$e = 0.2$	$e = 0.4$	$e = 0.8$
		$a/M = 0.1$		
8	5°	6.090×10^{-6} (7.374×10^{-8})	5.804×10^{-6} (1.710×10^{-7})	3.087×10^{-6} (3.944×10^{-7})
	40°	4.911×10^{-6} (6.131×10^{-8})	4.711×10^{-6} (1.406×10^{-7})	2.583×10^{-6} (3.277×10^{-7})
	85°	3.159×10^{-6} (7.040×10^{-8})	3.083×10^{-6} (1.377×10^{-7})	1.870×10^{-6} (3.020×10^{-7})
25	5°	8.592×10^{-8} (5.985×10^{-11})	7.473×10^{-8} (5.243×10^{-11})	2.639×10^{-8} (3.159×10^{-11})
	40°	6.858×10^{-8} (4.877×10^{-11})	5.969×10^{-8} (4.352×10^{-11})	2.113×10^{-8} (2.693×10^{-11})
	85°	4.362×10^{-8} (4.689×10^{-11})	3.800×10^{-8} (5.321×10^{-11})	1.349×10^{-8} (4.292×10^{-11})
		$a/M = 0.5$		
8	5°	5.610×10^{-6} (1.626×10^{-7})	5.014×10^{-6} (1.577×10^{-7})	2.049×10^{-6} (9.286×10^{-8})
	40°	4.698×10^{-6} (1.535×10^{-7})	4.275×10^{-6} (1.363×10^{-7})	1.856×10^{-6} (8.634×10^{-8})
	85°	3.159×10^{-6} (1.659×10^{-7})	3.038×10^{-6} (2.326×10^{-7})	1.653×10^{-6} (2.877×10^{-7})
25	5°	8.472×10^{-8} (4.352×10^{-10})	7.328×10^{-8} (4.683×10^{-10})	2.537×10^{-8} (2.663×10^{-10})
	40°	6.815×10^{-8} (3.490×10^{-10})	5.912×10^{-8} (3.768×10^{-10})	2.067×10^{-8} (2.165×10^{-10})
	85°	4.364×10^{-8} (2.460×10^{-10})	3.801×10^{-8} (2.795×10^{-10})	1.349×10^{-8} (1.872×10^{-10})
		$a/M = 0.9$		
8	5°	5.242×10^{-6} (3.108×10^{-7})	4.509×10^{-6} (3.171×10^{-7})	1.605×10^{-6} (1.673×10^{-7})
	40°	4.498×10^{-6} (2.570×10^{-7})	3.954×10^{-6} (2.691×10^{-7})	1.509×10^{-6} (1.548×10^{-7})
	85°	3.145×10^{-6} (2.784×10^{-7})	2.967×10^{-6} (3.706×10^{-7})	1.455×10^{-6} (3.746×10^{-7})
25	5°	8.360×10^{-8} (7.850×10^{-10})	7.193×10^{-8} (8.461×10^{-10})	2.444×10^{-8} (4.846×10^{-10})
	40°	6.769×10^{-8} (6.302×10^{-10})	5.852×10^{-8} (6.816×10^{-10})	2.021×10^{-8} (3.946×10^{-10})
	85°	4.361×10^{-8} (4.416×10^{-10})	3.798×10^{-8} (5.012×10^{-10})	1.347×10^{-8} (3.345×10^{-10})

For highly inclined orbits ($\theta_{\rm inc} = 85°$), the dominant contribution shifts to $k = 2$ for $n \lesssim 30$.

At fixed k, the location of the peak in the n spectrum exhibits only a weak dependence on inclination. At $a/M = 0.5$ and moderate eccentricity ($e = 0.2$), the dominant contribution to the energy flux at infinity always arises from the $(n, k) = (0, 0)$ mode, independently of the inclination angle. At higher eccentricity ($e = 0.8$), the position of the dominant peak depends on inclination, with the leading contribution corresponding to $k = 0$ and $n = 5, 6,$ and 9 for $\theta_{\rm inc} = 5°$, 40°, and 85°, respectively. For the $k = 2$ harmonic at $e = 0.8$, the dominant contribution in n varies only mildly—from $n = 34$ to $n = 36$—despite the large change in inclination. A similar weak dependence on inclination is observed for the energy flux absorbed at the horizon.

These features can be exploited in the construction of flux grids for the evolution of asymmetric binaries, providing practical guidance for the choice of summation strategies over the harmonic indices.

C. Dependence on black-hole spin

To characterize the dependence of the energy flux on the BH spin, we compare scalar energy spectra computed at different values of a/M, while keeping $(p/M, e, \theta_{\rm inc})$ fixed. We find that the modal structure is remarkably insensitive to the spin. As a general feature, the distribution in n remains nearly unchanged across the sampled values of a, while the width of the spectrum in k increases only mildly at high spin.

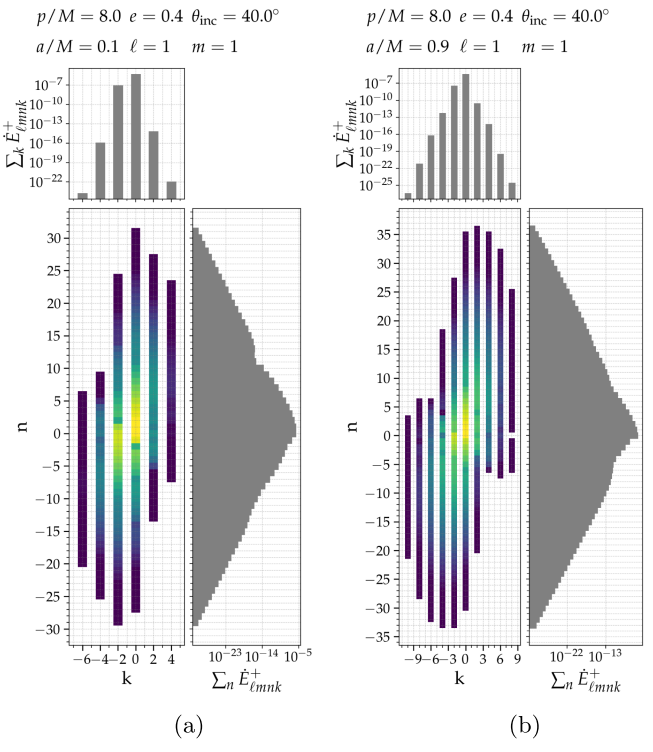


FIG. 5. Spectrum of the scalar energy flux emitted at infinity for the $(\ell, m) = (1, 1)$ harmonic. The binary parameters are $(e, p/M, \theta_{\rm inc}) = (0.4, 8, 40°)$. The left and right panels correspond to primary spins $a/M = 0.1$ and $a/M = 0.9$, respectively. The layout of the panels follows the same format as Fig. 4. (a) Scalar flux at infinity and (b) scalar flux at infinity.

As a representative example, Fig. 5 shows the flux at infinity for $(p/M, e, \theta_{\rm inc}) = (8, 0.4, 40°)$ and two values of the spin, $a/M = 0.1$ and $a/M = 0.9$. In both cases, the emission is dominated by the $k = 0$ modes with $n = 0$, 1, while all other contributions are suppressed by at least 1 order of magnitude.

A broader exploration of the parameter space (see Appendix D) indicates that the spin can induce a modest shift in the location of the spectral peak at higher eccentricity. For instance, at $(p/M, e, \theta_{\rm inc}) = (8, 0.8, 40°)$, the dominant contribution corresponds to $(k, n) = (0, 8)$ for $a/M = 0.1$, while it shifts to $(k, n) = (0, 5)$ for $a/M = 0.9$.

Overall, the harmonic content of the scalar flux is far more strongly influenced by the orbital eccentricity and inclination than by the BH spin.

IV. CONCLUSION AND OUTLOOK

In this study, we have taken a concrete step toward the systematic modeling of asymmetric binaries in theories of gravity endowed with a massless scalar degree of freedom. Considering fully generic bound orbits, we have computed the scalar energy and angular-momentum fluxes both at infinity and across the horizon, resolving their complete harmonic structure over a broad region of parameter space.

By decomposing the scalar field into frequency-domain modes labeled by the indices (ℓ, m, n, k), we have characterized the distribution of power across the scalar spectrum and identified the hierarchy of contributions that governs the emission. The radiation is predominantly dipolar, with the $\ell = m = 1$ mode providing the leading contribution to the total flux. Higher multipoles are progressively suppressed with increasing ℓ, yet they remain non-negligible, especially for eccentric and inclined configurations where the spectral content broadens and subdominant harmonics become comparatively enhanced. Accurate flux modeling therefore requires retaining these additional modes, as illustrated in Fig. 2.

Focusing on the $\ell = m = 1$ component, we have mapped the structure of the spectrum in the (n, k) plane. Eccentricity leads to a broadening of the distribution of the radial harmonic index n in the flux, shifting the spectral peak away from $n = 0$ at high e, while inclination affects the distribution in the polar index k, increasing the number of contributing harmonics without qualitatively altering the dominance of low-k modes. The BH spin, by contrast, affects the harmonic structure only mildly, inducing at most modest shifts in the location of the dominant peaks. These systematic trends provide practical guidance for constructing flux grids and optimizing harmonic summations in waveform models.

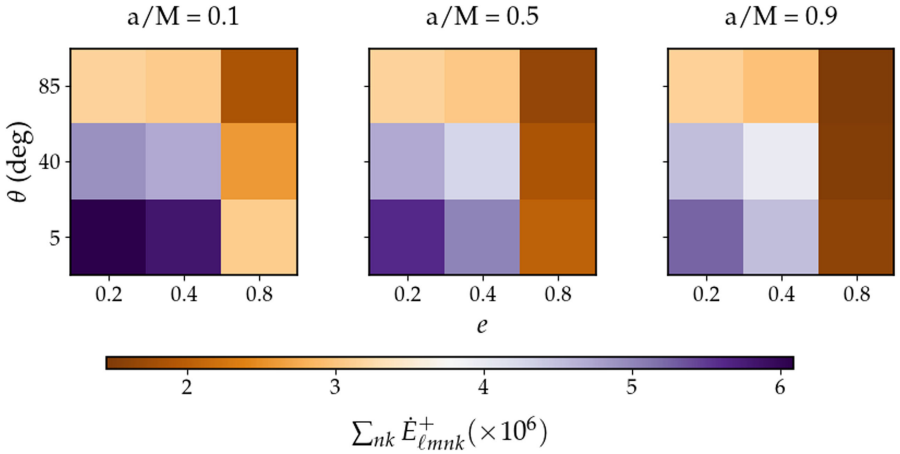


FIG. 6. Scalar energy flux (in units of 10^{-6}) emitted at infinity by binaries at fixed orbital radius, $p/M = 8$ shown as a function of eccentricity e (horizontal axis) and inclination $\theta_{\rm inc}$ (vertical axis), for three values of the spin parameter a/M, for $\ell = m = 1$. Each panel corresponds to a different spin. The color scale indicates the magnitude of the flux, with a common normalization across all panels to allow direct comparison.

Figure 6 offers a global view of the total scalar energy flux emitted at infinity for $p/M = 8$, as a function of eccentricity, inclination, and spin. As also quantified in Table V, the overall magnitude of the flux varies only moderately across the sampled configurations. While the detailed spectral distribution is significantly affected even by small changes in the orbital geometry, the total emitted power remains within a relatively narrow range, and the same qualitative behavior is observed in the fluxes absorbed at the horizon.

Since the instantaneous flux at a given orbital radius exhibits limited variation across the geometric parameter space, the impact of scalar charge constraints on the binary geometry will then depend on the cumulative effect of scalar radiation over the full inspiral, and on the coupled evolution of eccentricity, inclination, and orbital radius.

The results presented here provide the essential building blocks for investigating the long-term evolution and waveform generation of scalar-charged EMRIs and IMRIs. In our framework, the resulting waveforms are exact at the adiabatic order, i.e., at first order in the perturbative expansion. Achieving this level of accuracy requires the construction of dense grids of scalar amplitudes and fluxes as functions of the orbital parameters, in close analogy with the infrastructure underlying state-of-the-art models in GR. The analysis carried out in this work delivers precisely the information needed to build such grids in the scalar sector.

More broadly, although our primary motivation is precision modeling of asymmetric binaries beyond GR, the numerical framework developed here can also serve as a validated tool for high-accuracy flux computations within GR itself, thereby contributing to the refinement of perturbative modeling in both contexts.

The next stage of our research program using EMRIs and IMRIs to probe fundamental physics is the incorporation of the scalar amplitude and flux grids into inspiral and waveform-generation frameworks, such as `FEW` [97–99]. In a forthcoming companion work, we will implement the grids within an adiabatic inspiral scheme, enabling consistent orbital evolution and parameter-estimation studies for scalar-charged EMRIs and IMRIs.

While the fluxes computed here capture the instantaneous emission for given orbital configurations, assessing in full LISA's ability to constrain the scalar charge requires modeling the cumulative effect of scalar radiation over the complete inspiral. Embedding these results into an inspiral framework will allow us to explore the parameter space of asymmetric binaries and identify configurations that maximize sensitivity to scalar charge, including potential "golden" systems arising from specific combinations of spin, eccentricity, and inclination. Extending this analysis to larger mass ratios will also be of interest, particularly to assess whether the merger phase may contribute non-negligibly to the observable signal [47].

ACKNOWLEDGMENTS

M. D. R. is supported by the MUR FIS2 Advanced Grant No. ET-NOW (CUP: B53C25001080001) and by the INFN TEONGRAV initiative. A. M. acknowledges financial support from MUR PRIN Grants No. 2022-Z9X4XS and No. 2020KB33TP. T. P. S. acknowledges partial support from the STFC Consolidated Grants No. ST/V005596/1, No. ST/X000672/1, and No. UKRI2492.

DATA AVAILABILITY

C++ code publicly available at this GitHUb repository: [59].

APPENDIX A: ELLIPTIC INTEGRALS

We show here the form of the elliptic integrals used in Sec. II B to determine a solution for Kerr geodesics. The integral of the first kind is given by

$$\mathrm{F}(\phi|m) = \int_0^{\phi} (1 - m\sin^2\theta)^{-1/2} \mathrm{d}\theta, \tag{A1}$$

for real m, $-\pi/2 < \phi < \pi/2 <$, $m\sin^2\phi < 1$. This function is the inverse of the Jacobi amplitude

$$\phi = \mathrm{am}(u|\phi) \quad \text{with} \quad u = F(\phi|m), \qquad m < 1. \tag{A2}$$

When $\phi = \pi/2$, we get the complete elliptic integral of the first kind,

$$\mathrm{K}(m) = F(\pi/2|m). \tag{A3}$$

The elliptic integral of the second kind is

$$\mathrm{E}(\phi|m) = \int_0^{\phi} (1 - m\sin^2\theta)^{1/2} \mathrm{d}\theta, \tag{A4}$$

for $m < 1$, $-\pi/2 < \phi < \pi/2 <$. When $\phi = \pi/2$, we get the complete elliptic integral of the second kind,

$$\mathrm{E}(m) = E(\pi/2|m). \tag{A5}$$

Finally, the elliptic integral of the third kind is

$$\Pi(n;\phi|m) = \int_0^{\phi} (1 - n\sin^2\theta)^{-1} (1 - m\sin^2\theta)^{-1/2} \mathrm{d}\theta, \tag{A6}$$

for real m, n, $-\pi/2 < \phi < \pi/2 <$ and $m\sin^2\phi < 1$. When $\phi = \pi/2$, we get the complete elliptic integral of the third kind,

$$\Pi(n|m) = \Pi(n;\pi/2|m). \tag{A7}$$

APPENDIX B: FUNCTIONS DESCRIBING THE ORBITAL MOTION

We collect here the explicit expressions for the orbital motion functions introduced in Sec. II B. The expressions defined in Eq. (37) are

$$\begin{aligned}\tilde{t}_r(\xi_r) = {} & \frac{\mathcal{E}(r_2 - r_3)}{\sqrt{(1-\mathcal{E}^2)(r_1 - r_3)(r_2 - r_4)}} \\ & \times \left\{ (4 + r_1 + r_2 + r_3 + r_4)\Pi(h_r;\xi_r|k_r) \right. \\ & - \frac{4}{r_+ - r_-} \left(\frac{r_+(4 - a\mathcal{L}/\mathcal{E}) - 2a^2}{(r_2 - r_+)(r_3 - r_+)} \right. \\ & \left. \times \Pi(h_+;\xi_r|k_r) - (+ \leftrightarrow -) \right) + \frac{(r_1 - r_3)(r_2 - r_4)}{r_2 - r_3} \\ & \left. \times \left(\mathrm{E}(\xi_r|k_r) - h_r \frac{\sqrt{1 - k_r\sin^2\xi_r}\sin\xi_r\cos\xi_r}{1 - h_r\sin^2\xi_r} \right) \right\},\end{aligned} \tag{B1}$$

$$\tilde{t}_z(\xi_z) = -\frac{\mathcal{E}}{1-\mathcal{E}^2} z_2 \mathrm{E}(\xi_z|k_z), \tag{B2}$$

The expressions defined in Eq. (39) are

$$\begin{aligned}\tilde{\phi}_r(\xi_r) = {} & -\frac{2a\mathcal{E}(r_2 - r_3)}{(r_+ - r_-)\sqrt{(1-\mathcal{E}^2)(r_1 - r_3)(r_2 - r_4)}} \\ & \times \left(\frac{2r_+ - a\mathcal{L}/\mathcal{E}}{(r_2 - r_+)(r_3 - r_+)} \Pi(h_+;\xi_r|k_r) - (+ \leftrightarrow -) \right),\end{aligned} \tag{B3}$$

$$\tilde{\phi}_z(\xi_z) = \frac{\mathcal{L}}{z_2} \Pi(z_1^2;\xi_z|k_z), \tag{B4}$$

where

$$h_r = \frac{r_1 - r_2}{r_1 - r_3}, \qquad h_\pm = h_r \frac{r_3 - r_\pm}{r_2 - r_\pm}. \tag{B5}$$

The expressions defined in Eq. (40) are

$$\begin{aligned}\tilde{\Upsilon}_{\phi,r} = {} & \frac{a}{r_+ - r_-} \left(\frac{2\mathcal{E}r_+ - a\mathcal{L}}{r_3 - r_+} \right. \\ & \left. \times \left(1 - \frac{r_2 - r_3}{r_2 - r_+} \frac{\Pi(h_+|k_r)}{\mathrm{K}(k_r)} \right) - (+ \leftrightarrow -) \right),\end{aligned} \tag{B6}$$

$$\tilde{\Upsilon}_{\phi,z} = \frac{\mathcal{L}}{\mathrm{K}(k_z)} \Pi(z_1^2|k_z), \tag{B7}$$

$$\tilde{\Upsilon}_{t,r} = (4+a^2)\mathcal{E} + \mathcal{E}\left(\frac{1}{2}\left((4+r_1+r_2+r_3)r_3 - r_1r_2 + (r_1-r_3)(r_2-r_4)\frac{\mathrm{E}(k_r)}{\mathrm{K}(k_r)} + (4+r_1+r_2+r_3+r_4)(r_2-r_3)\frac{\Pi(h_r|k_r)}{\mathrm{K}(k_r)}\right) + \frac{2}{r_+-r_-}\left(\frac{(4-a\mathcal{L}/\mathcal{E})r_+ - 2a^2}{r_3-r_+} \times \left(1-\frac{r_2-r_3}{r_2-r_+}\frac{\Pi(h_+|k_r)}{\mathrm{K}(k_r)}\right) - (+\leftrightarrow -)\right)\right), \quad \text{(B8)}$$

$$\tilde{\Upsilon}_{t,z} = -a^2\mathcal{E} + \frac{\mathcal{E}\mathcal{Q}}{(1-\mathcal{E}^2)z_1^2}\left(1-\frac{\mathrm{E}(k_z)}{\mathrm{K}(k_r)}\right). \quad \text{(B9)}$$

Here, E and Π are the elliptic functions defined in Appendix A.

APPENDIX C: NUMERICAL IMPLEMENTATION OF THE CODE

We describe the mathematical techniques implemented in STORM [59] to solve the angular and radial Teukolsky equations.

1. Spin-weighted spheroidal harmonics

The computation of the spin-weighted spheroidal harmonics

$$\mathcal{S}_{\ell m}(\omega,\theta,\phi) = S_{\ell m}(\omega,\theta)e^{im\phi},$$

is implemented in the `SpinWeightedSpheroidalHarmonics` class. These functions satisfy the angular Teukolsky equation for a generic spin weight s, as follows:

$$\left[\frac{1}{\sin\theta}\frac{\mathrm{d}}{\mathrm{d}\theta}\left(\sin\theta\frac{\mathrm{d}}{\mathrm{d}\theta}\right) + \zeta^2\cos^2\theta - 2s\zeta\cos\theta - \frac{(m+s\cos\theta)^2}{\sin^2\theta} + E_{\ell m}(\zeta) - s^2\right]S_{\ell m}(\omega,\theta) = 0, \quad \text{(C1)}$$

where $\zeta = a\omega$ is the oblateness parameter. In our implementation, the continued-fraction procedure determines the angular separation constant $\lambda_{\ell m}$, which is related to the quantity $E_{\ell m}(\zeta)$ appearing in Eq. (C1) through

$$E_{\ell m}(\zeta) = \lambda_{\ell m} + s(s+1) - \zeta^2 + 2m\zeta. \quad \text{(C2)}$$

The class therefore solves Eq. (C1) by computing the separation constant $\lambda_{\ell m}$ and constructing the corresponding eigenfunctions for arbitrary spin weight s, multipole indices (ℓ, m), and oblateness parameter $\zeta = a\omega$.

a. Eigenvalue computation

To determine the eigenvalue, the class employs a continued-fraction approach, following Ref. [100]. The solution of the angular Teukolsky equation is expanded in terms of Jacobi polynomials, leading to a three-term recurrence relation for the series coefficients a_n, as follows:

$$\alpha_n a_{n+1} + \beta_n a_n + \gamma_n a_{n-1} = 0, \quad \text{(C3)}$$

where the coefficients α_n, β_n, and γ_n depend on (s,ℓ,m,ζ) and on the eigenvalue ${}_sE_{\ell m}(\zeta)$ (we refer the reader to Ref. [100] for their explicit expressions). Defining the ratios

$$R_n = \frac{a_n}{a_{n-1}}, \qquad L_n = \frac{a_n}{a_{n+1}}, \quad \text{(C4)}$$

the recurrence relation can be recast as a continued-fraction condition,

$$\beta_n + \alpha_n R_{n+1} + \gamma_n L_{n-1} = 0, \quad \text{(C5)}$$

which is solved using a root-finding algorithm, yielding the eigenvalue

$$\lambda_{\ell m} = E_{\ell m}(\zeta) - s(s+1) + \zeta^2 - 2m\zeta, \quad \text{(C6)}$$

to the desired precision.

In the limits of low and high oblateness, i.e., $\zeta \ll 1$ and $\zeta \gg 1$, respectively, perturbative analytic expansions provide sufficiently accurate initial guesses [100,101]. However, these expansions lose accuracy in the intermediate regime. In contrast, the spectral method based on spherical-harmonic expansions provides a robust initial estimate at any ζ [102]. In this approach, the spin-weighted spheroidal harmonics are expanded in a truncated basis of spin-weighted spherical harmonics, and the angular Teukolsky equation is projected onto this basis, yielding a finite-dimensional symmetric matrix eigenvalue problem. The eigenvalues of this matrix are computed using the classical Jacobi rotation method for symmetric matrices (see, e.g., Ref. [103]). The eigenvalue corresponding to the desired ℓ is then selected as an accurate initial guess [102]. Finally, a Newton-Raphson algorithm is used to refine the eigenvalue iteratively to the target precision.

b. Angular function evaluation

Once the eigenvalue $E_{\ell m}(\zeta)$ is determined, the spin-weighted spheroidal harmonic is constructed using Leaver's method [104]. In this approach, the recurrence relation is expressed in powers of $(1+\cos\theta)$ rather than Jacobi polynomials, so that the recurrence coefficients $\tilde{\alpha}_n$, $\tilde{\beta}_n$, and $\tilde{\gamma}_n$ differ from those in the continued-fraction method [104].

The spheroidal harmonic is then given by

$$\mathcal{S}_{\ell m}(\omega,\theta) = \mathcal{N} e^{a\omega\cos\theta}(1+\cos\theta)^{k_1}(1-\cos\theta)^{k_2} \times \sum_{n=0}^{N_{\max}} \tilde{a}_n (1+\cos\theta)^n, \tag{C7}$$

where $k_1 = |m-s|/2$, $k_2 = |m+s|/2$, and $\mathcal{N}$ is a normalization constant.

In practice, the coefficients $\tilde{a}_n$ are generated iteratively using the three-term recurrence relation. The normalization constant is then determined by enforcing the orthonormality condition in Eq. (58), and the overall sign is fixed to ensure continuity with the spherical-harmonic limit. This class also computes the first and second derivatives of $\mathcal{S}_{\ell m}(\omega,\theta,\phi)$ with respect to θ, needed for gravitational energy-flux calculations. This procedure yields a fully normalized, numerically stable representation of the spin-weighted spheroidal harmonics, suitable for both scalar and gravitational perturbations.

2. Homogeneous radial function

The class `RadialHomogeneousSolution` computes the two linearly independent homogeneous solutions of the radial Teukolsky equation, which are required to construct the corresponding Green's function solution and to evaluate the fluxes at the horizon and at infinity for arbitrary spin weight s, as follows:

$$\Delta^{-s}\frac{\mathrm{d}}{\mathrm{d}r}\left(\Delta^{s+1}\frac{\mathrm{d}R_{\ell m}}{\mathrm{d}r}\right) + V R_{\ell m} = 0, \tag{C8}$$

with potential

$$V = \frac{K^2 - 2is(r-M)K}{\Delta} + 4is\omega r - \lambda_{\ell m}, \tag{C9}$$

where

$$K = (r^2+a^2)\omega - am, \tag{C10}$$

and $\lambda_{\ell m}$ is the angular separation constant defined in Eq. (C2).

The class computes the purely ingoing (outgoing) solution $\tilde{R}^{-}_{\ell m}$ ($\tilde{R}^{+}_{\ell m}$) at the horizon (infinity) using a hybrid numerical-analytical scheme based on the Mano-Suzuki-Takasugi (MST) formalism [105]. In this work, we adopt the normalization convention defined in Eqs. (67) and (68), such that $\tilde{R}^{-}_{\ell m}$ is purely ingoing at the horizon with unit amplitude, while $\tilde{R}^{+}_{\ell m}$ is purely outgoing at infinity with unit amplitude.

With this choice, the normalized solutions $\tilde{R}^{\pm}_{\ell m}$ are related to the standard MST solutions $R^{\mathrm{in}}_{\ell m}$ and $R^{\mathrm{up}}_{\ell m}$ via [106]

$$\tilde{R}^{+} = \frac{R^{\nu}_{\mathrm{up}}}{C^{\mathrm{trans}}}, \qquad \tilde{R}^{-} = \frac{R^{\nu}_{\mathrm{in}}}{B^{\mathrm{trans}}}, \tag{C11}$$

where C^{trans} and B^{trans} are normalization constants and ν is the so-called *renormalized angular momentum* [105], i.e., the extra parameter introduced in the MST method to allow for a convergent series representation of the functions $R^{\mathrm{in,up}}$. Here and thereafter, we suppress the (ℓ, m) indices when no ambiguity arises.

The class also provides a routine to compute the Wronskian defined in Eq. (70) via

$$A^{\mathrm{in}} = \frac{B^{\mathrm{inc}}}{B^{\mathrm{trans}}}, \tag{C12}$$

where B^{inc} is the incident amplitude at spatial infinity of R^{in} [106].

The class also provides routines to compute the first and second radial derivatives of $R^{\pm}$. These derivatives are obtained analytically from the MST series representations, using the known derivative relations of the hypergeometric and confluent hypergeometric functions. They are required for the evaluation of gravitational fluxes at the horizon and at infinity, ensuring that the fluxes are computed with the same high accuracy as the radial functions themselves.

a. MST method

The MST method provides a series representation of the amplitudes B^{trans}, C^{trans}, and B^{inc}, i.e., Ref. [106], as follows:

$$\begin{aligned} B^{\mathrm{trans}} &= \left(\frac{\epsilon\kappa}{\omega}\right)^{2s} e^{i\kappa\epsilon_+\left(1+\frac{2\ln\kappa}{1+\kappa}\right)} \sum_{n=-\infty}^{\infty} f^{\nu}_n, \\ C^{\mathrm{trans}} &= \omega^{-1-2s} e^{-i(\epsilon\ln\epsilon - \frac{1-\kappa}{2}\epsilon)} A^{\nu}_{-}, \\ B^{\mathrm{inc}} &= \omega^{-1}\left[K_\nu - ie^{-i\pi\nu}\frac{\sin\pi(\nu-s+i\epsilon)}{\sin\pi(\nu+s-i\epsilon)}K_{-\nu-1}\right] \\ &\quad \times A^{\nu}_{+} e^{-i(\epsilon\ln\epsilon - \frac{1-\kappa}{2}\epsilon)}, \end{aligned} \tag{C13}$$

and the solutions R^{ν}_{up} and R^{ν}_{in} as

$$\begin{aligned} R^{\nu}_{\mathrm{up}} &= 2^{\nu} e^{-\pi\epsilon} e^{-i\pi(\nu+1+s)} e^{i\hat{z}} \hat{z}^{\nu+i\epsilon_+} (\hat{z}-\epsilon\kappa)^{-s-i\epsilon_+} \\ &\quad \times \sum_{n=-\infty}^{\infty} i^n \frac{(\nu+1+s-i\epsilon)_n}{(\nu+1-s+i\epsilon)_n} f^{\nu}_n (2\hat{z})^n \\ &\quad \times \Psi(n+\nu+1+s-i\epsilon, 2n+2\nu+2; -2i\hat{z}), \end{aligned} \tag{C14}$$

and

$$R^{\nu}_{\mathrm{in}} = R^{\nu}_0 + R^{-\nu-1}_0, \tag{C15}$$

with

$$R_0^\nu = e^{i\epsilon\kappa x}(-x)^{-s-\frac{i}{2}(\epsilon+\tau)}(1-x)^{\frac{i}{2}(\epsilon+\tau)+\nu} \times \sum_{n=-\infty}^{\infty} f_n^\nu \frac{\Gamma(1-s-i\epsilon-i\tau)\Gamma(2n+2\nu+1)}{\Gamma(n+\nu+1-i\tau)\Gamma(n+\nu+1-s-i\epsilon)} \times F\left(-n-\nu-i\tau,-n-\nu-s-i\epsilon;-2n-2\nu;\frac{1}{1-x}\right) \times (1-x)^n. \tag{C16}$$

Here, Ψ is the irregular confluent hypergeometric function, F is regular hypergeometric function, and

$$x = \frac{\omega(r_+ - r)}{\epsilon\kappa}, \qquad \epsilon = 2M\omega,$$
$$\kappa = \sqrt{1-\left(\frac{a}{M}\right)^2}, \qquad \tau = \frac{\epsilon - m(a/M)}{\kappa},$$
$$\hat{z} = \omega(r-r_-), \qquad \epsilon_+ = (\epsilon+\tau)/2, \tag{C17}$$

$$A_-^\nu = 2^{-1-s+i\epsilon}e^{-\frac{\pi}{2}i(\nu+1+s)}e^{-\frac{\pi}{2}\epsilon} \times \sum_{n=-\infty}^{\infty}(-1)^n \frac{(\nu+1+s-i\epsilon)_n}{(\nu+1-s+i\epsilon)_n} f_n^\nu, \tag{C18}$$

$$A_+^\nu = e^{-\frac{\pi}{2}\epsilon}e^{\frac{\pi}{2}i(\nu+1-s)}2^{-1+s-i\epsilon} \times \frac{\Gamma(\nu+1-s+i\epsilon)}{\Gamma(\nu+1+s-i\epsilon)} \sum_{n=-\infty}^{\infty} f_n^\nu, \tag{C19}$$

$$K_\nu = \frac{e^{i\epsilon\kappa}(2\epsilon\kappa)^{s-\nu-r}2^{-s}i^r\Gamma(1-s-2i\epsilon_+)}{\Gamma(r+\nu+1-s+i\epsilon)\Gamma(r+\nu+1+i\tau)} \times \frac{\Gamma(r+2\nu+2)}{\Gamma(r+\nu+1+s+i\epsilon)} \times \left(\sum_{n=r}^{\infty}(-1)^n \frac{\Gamma(n+r+2\nu+1)}{(n-r)!} \times \frac{\Gamma(n+\nu+1+s+i\epsilon)}{\Gamma(n+\nu+1-s-i\epsilon)}\frac{\Gamma(n+\nu+1+i\tau)}{\Gamma(n+\nu+1-i\tau)} f_n^\nu\right) \times \left(\sum_{n=-\infty}^{\infty} r\frac{(-1)^n}{(r-n)!(r+2\nu+2)_n} \times \frac{(\nu+1+s-i\epsilon)_n}{(\nu+1-s+i\epsilon)_n} f_n^\nu\right)^{-1}. \tag{C20}$$

Finally, the coefficients f_n^ν are determined by the three-term recurrence relation

$$\alpha_n^\nu f_{n+1}^\nu + \beta_n^\nu f_n^\nu + \gamma_n^\nu f_{n-1}^\nu = 0, \tag{C21}$$

where the coefficients α_n^ν, β_n^ν, and γ_n^ν depend on the mode parameters (ℓ, m, ω, s) and are given explicitly in Ref. [106].

The physically relevant sequence $\{f_n^\nu\}$ corresponds to the minimal solution of the recurrence relation in both the $n \to +\infty$ and $n \to -\infty$ directions. This requirement ensures convergence of the hypergeometric and Coulomb series representations. The condition for minimality can be written as

$$g_n(\nu) = \beta_n^\nu + \alpha_n^\nu R_{n+1} + \gamma_n^\nu L_{n-1} = 0, \tag{C22}$$

where $R_n = f_n/f_{n-1}$ and $L_n = f_n/f_{n+1}$ are expressed as continued fractions derived from the recurrence relation. Since the choice of n is arbitrary, we set $n = 0$ in practice. The continued fractions entering R_n and L_n are evaluated using the continued-fraction routines provided by the Boost C++ library.

The class `RadialHomogeneousSolution` provides two strategies for computing ν:

(1) A Newton-Raphson iteration in the complex plane applied to the function $g_n(\nu)$ defined in Eq. (C22).
(2) The *monodromy method* [107], which expresses ν in terms of the monodromy data of the Teukolsky radial solution.

The Newton-Raphson approach is generally more efficient at low frequencies, whereas the monodromy method is required at high frequencies. In both cases, the iterative procedures are controlled by user-defined tolerance parameters, allowing the desired numerical accuracy to be specified at runtime. This ensures convergence of the continued-fraction solution and gives the user full control over the trade-off between accuracy and computational cost.

After determining the renormalized angular momentum, the coefficients f_n^ν can be computed.

From a technical standpoint, all infinite sums over n appearing in the MST series representations are evaluated using a symmetric truncation strategy about $n = 0$. At each iteration, the contributions from the positive and negative indices $+n$ and $-n$ are computed simultaneously and added to the partial sum.

The summation is terminated once the relative magnitude of the newly added terms, measured with respect to the accumulated sum, falls below a prescribed numerical tolerance for a fixed number of consecutive iterations. Requiring several consecutive subthreshold contributions prevents premature termination due to accidental cancellations or oscillatory behavior of the series.

This procedure ensures controlled convergence and uniform accuracy across the parameter space, providing analytically accurate boundary data that are subsequently used in the hybrid numerical-analytical integration scheme described below.

b. Hybrid numerical-analytical scheme

Although the MST series provides an exact analytic representation, its direct evaluation at every radial point is

computationally expensive. To improve efficiency, the class implements a hybrid numerical-analytical scheme following Ref. [108]: the MST formalism is used only to set accurate boundary conditions near the horizon and at infinity, while the radial Teukolsky equation is integrated numerically in the interior region.

To ensure that this numerical integration remains stable and efficient across the full domain between the horizon and infinity, it is convenient to introduce a new radial function φ, related to the Teukolsky solution R by

$$\varphi = r\Delta^{-s}e^{-im\tilde{\phi}}e^{-i\omega h}R, \tag{C23}$$

and to redefine the angular variable ϕ via

$$\mathrm{d}\tilde{\phi} = \mathrm{d}\phi + \frac{a}{r^2+a^2}\mathrm{d}r_\star. \tag{C24}$$

These transformations cast the Teukolsky equation into a form with a short-ranged effective potential, as follows:

$$\frac{(r^2+a^2)^2}{r^4}\frac{\mathrm{d}^2\varphi}{\mathrm{d}r_\star^2} - \frac{2\tilde{G}}{r^5}\frac{\mathrm{d}\varphi}{\mathrm{d}r_\star} + \frac{\tilde{U}}{r^6}\varphi = 0, \tag{C25}$$

where

$$\tilde{G} = a^2\Delta + (r^2+a^2)\{rs(r-M) - ir[(r^2+a^2)\omega H + ma]\}, \tag{C26}$$

and

$$\begin{aligned}\tilde{U} = {} & 2is\omega r^2(r\Delta(1-H) - M(r^2-a^2)(1+H)) \\ & - 2iar\Delta(m + a\omega H) + \Delta(2a^2 - r^2\lambda - 2Mr(s+1)) \\ & - 2ma\omega r^2(r^2+a^2)(1+H) \\ & + r^2(r^2+a^2)^2(\omega^2(1-H^2) + i\omega H').\end{aligned} \tag{C27}$$

Here, $H = \mathrm{d}h/\mathrm{d}r_\star$ satisfies

$$|H| \le 1, \qquad \lim_{r_\star\to\pm\infty} H = \pm 1, \qquad \lim_{r_\star\to\pm\infty}\frac{\mathrm{d}H}{\mathrm{d}r_\star} = 0. \tag{C28}$$

In practice, the numerical integration is performed with user-controlled tolerance parameters that determine the step size and convergence criteria. This allows the user to balance numerical accuracy and computational efficiency, ensuring that the solution remains stable across the full radial domain while retaining high precision near the boundaries set by the MST series.

APPENDIX D: FLUXES

In this Appendix, we present the scalar spectra analyzed in Sec. III.

Figures 7, 8, 13, and 14 present the scalar spectra at the horizon and at infinity for different values of (ℓ, m), for a fixed orbital configuration with parameters $(a/M, p/M, e, \theta_{\rm inc}) = (0.3, 0.5, 7, 30°)$.

Figures 9, 10, 15, and 16 display 18 scalar spectra for the energy and angular momentum flux at the horizon and at infinity, respectively, illustrating how the (n,k) mode structure depends on $(p/M, e, \theta_{\rm inc})$ for fixed $(\ell, m) = (1,1)$ and black-hole spin $a/M = 0.9$. Each figure is organized into two 3×3 blocks: the upper block corresponds to $p/M = 8$, while the lower block corresponds to $p/M = 25$. Within each block, the rows represent eccentricities $e = 0.2, 0.4, 0.8$, and the columns represent orbital inclinations $\theta_{\rm inc} = 5°, 40°, 85°$.

Finally, Figs. 11, 12, 17, and 18 illustrate the dependence of the scalar spectra on the spin a of the primary BH. In these figures, we fix $(e, \theta_{\rm inc}) = (0.4, 40°)$ and consider two orbital radii, $p/M = 8, 25$. The rows correspond to the two values of p/M, while the three columns show results for spins $a/M = 0.1, 0.5, 0.9$.

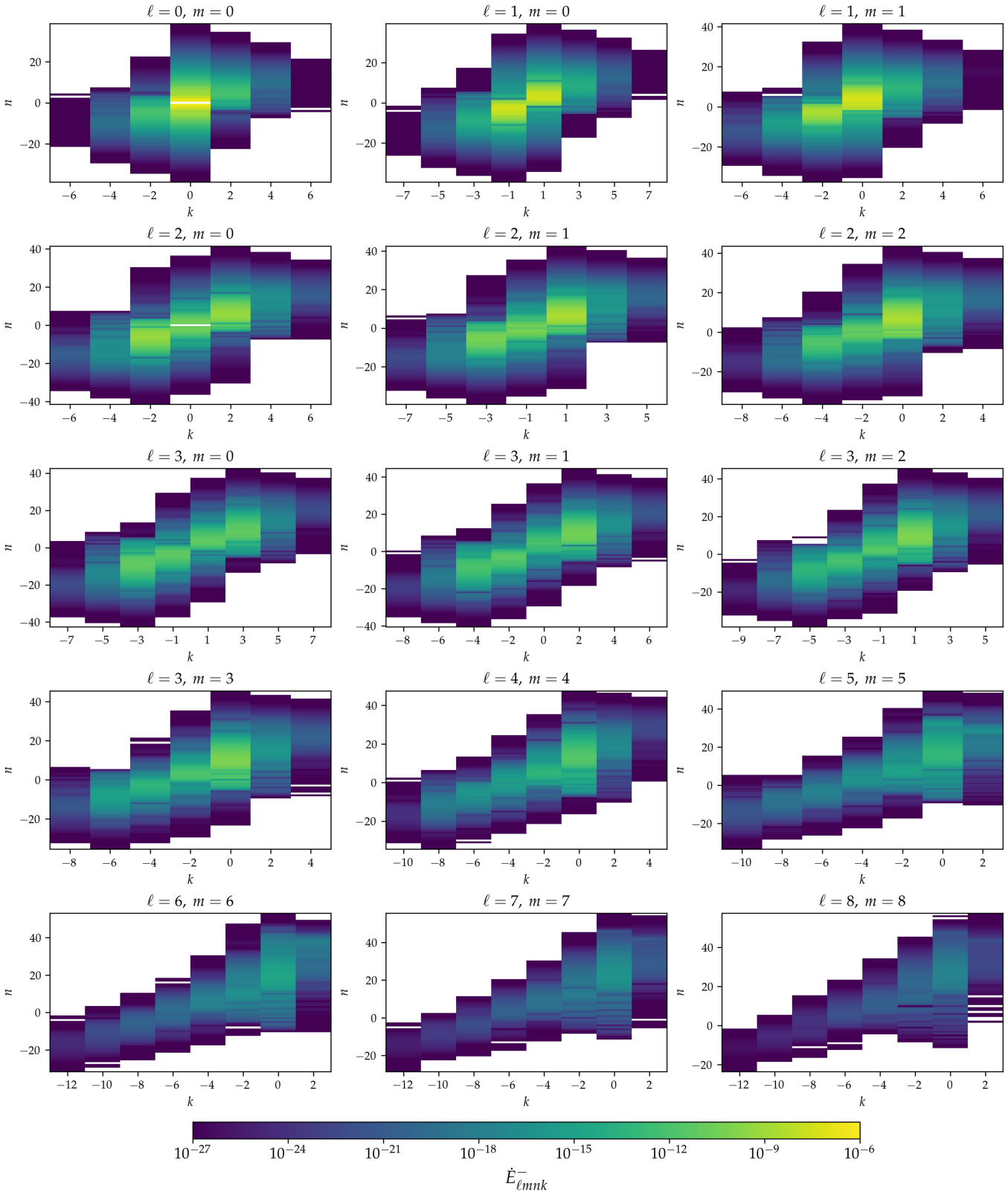


FIG. 7. Multipolar (n, k) components of the scalar spectra, $\dot{E}^{-}_{\ell mnk}$, at the horizon for varying ℓ and m, with fixed $a/M = 0.3$, $p/M = 7$, $e = 0.5$, and $\theta_{\rm inc} = 30°$. The color scale indicates the magnitude of the single-mode flux.

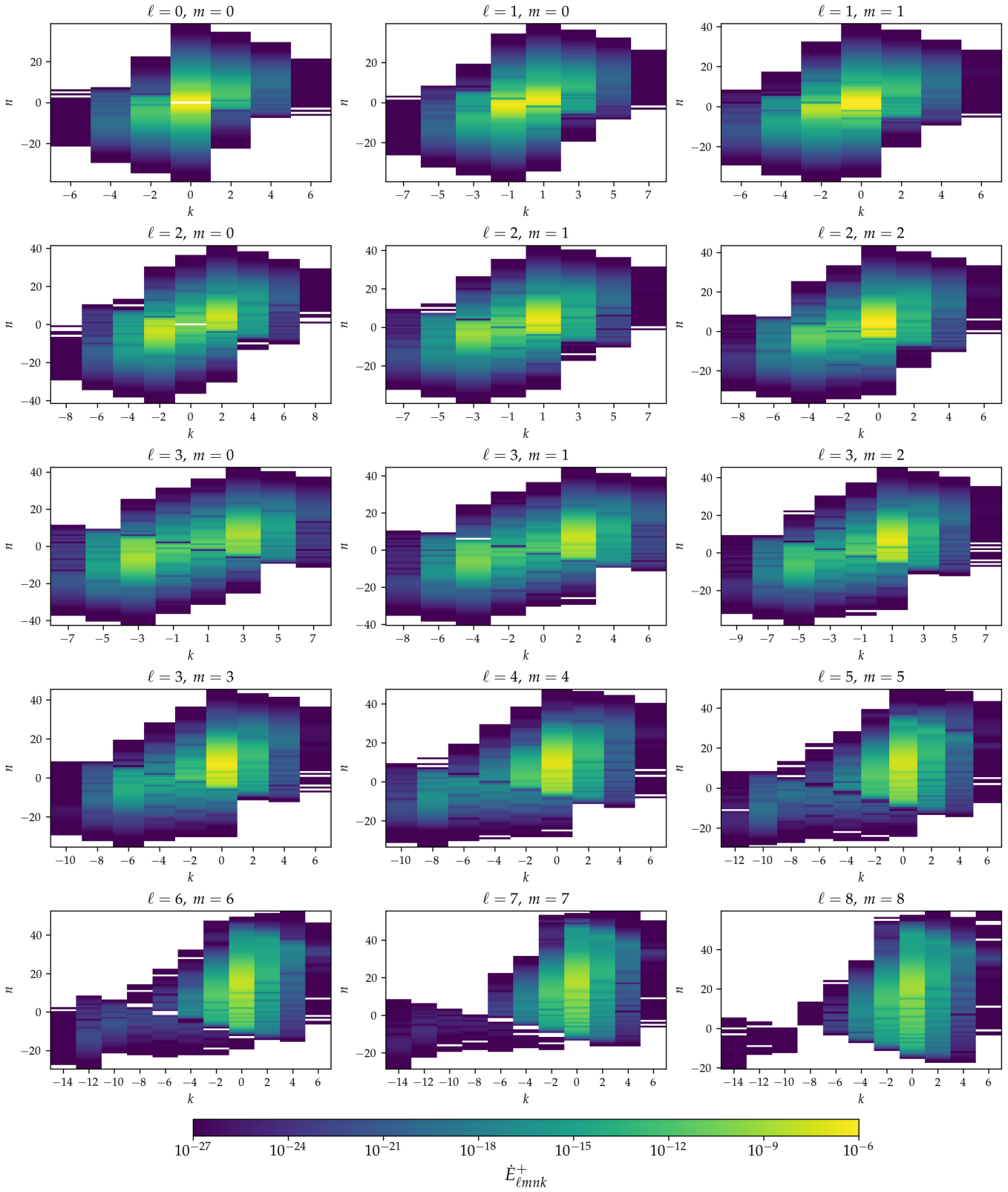


FIG. 8. Multipolar (n, k) components of the scalar spectra, $\dot{E}^{+}_{\ell mnk}$, at infinity for varying ℓ and m, with fixed $a/M = 0.3$, $p/M = 7$, $e = 0.5$, and $\theta_{\rm inc} = 30°$. The color scale indicates the magnitude of the single-mode flux.

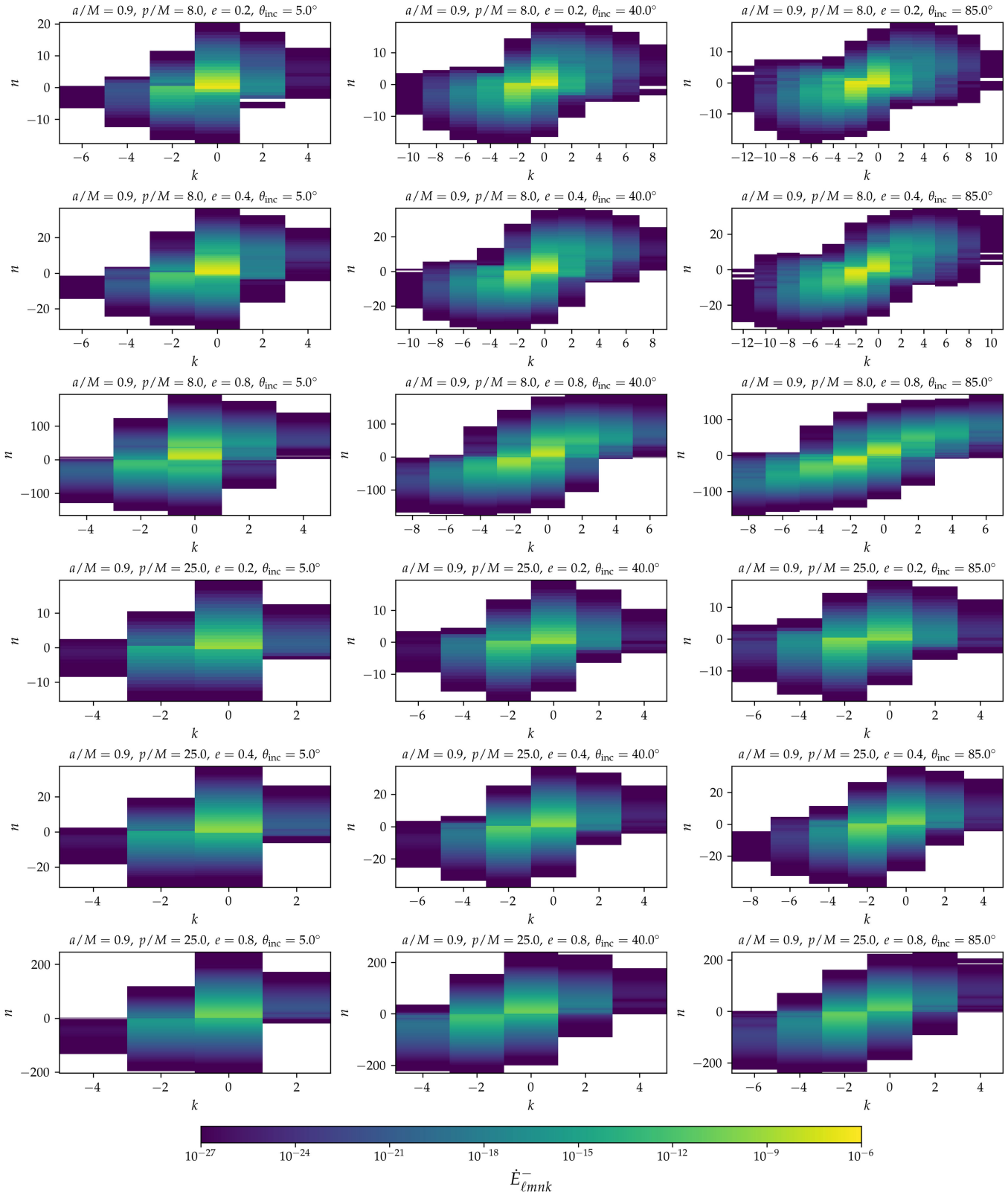


FIG. 9. Multipolar (n, k) components of the scalar spectra, $\dot{E}^{-}_{\ell mnk}$, at the horizon for varying p/M, e, and $\theta_{\rm inc}$, with fixed $a/M = 0.9$ and $\ell = m = 1$. The color scale indicates the magnitude of the single-mode flux.

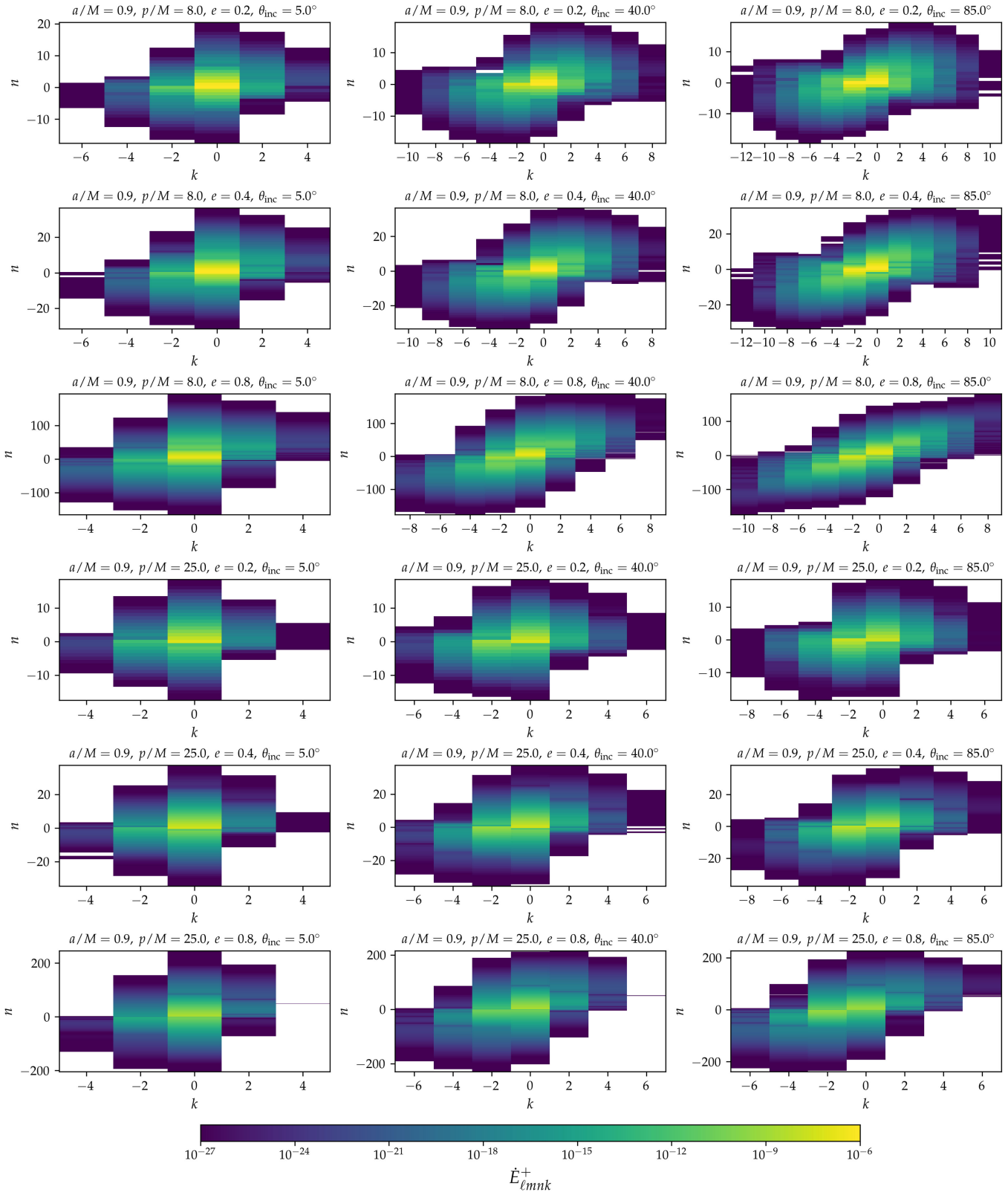


FIG. 10. Multipolar (n, k) components of the scalar spectra, $\dot{E}^{+}_{\ell mnk}$, at infinity for varying p/M, e, and $\theta_{\rm inc}$, with fixed $a/M = 0.9$ and $\ell = m = 1$. The color scale indicates the magnitude of the single-mode flux.

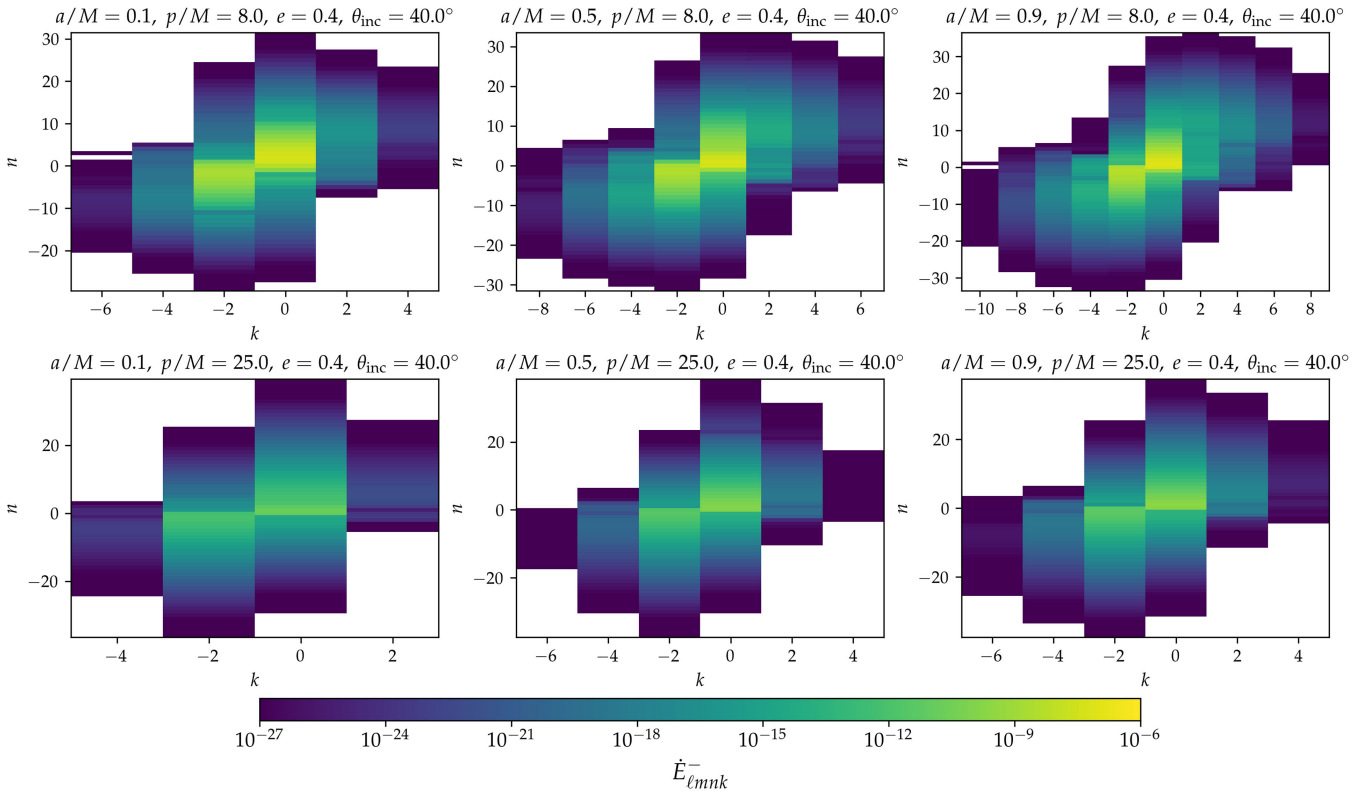


FIG. 11. Multipolar (n,k) components of the scalar spectra, $\dot{E}^{-}_{\ell mnk}$, at the horizon for varying a/M and p/M, with fixed $e = 0.4$, $\theta_{\rm inc} = 40°$, and $\ell = m = 1$. The color scale indicates the magnitude of the single-mode flux.

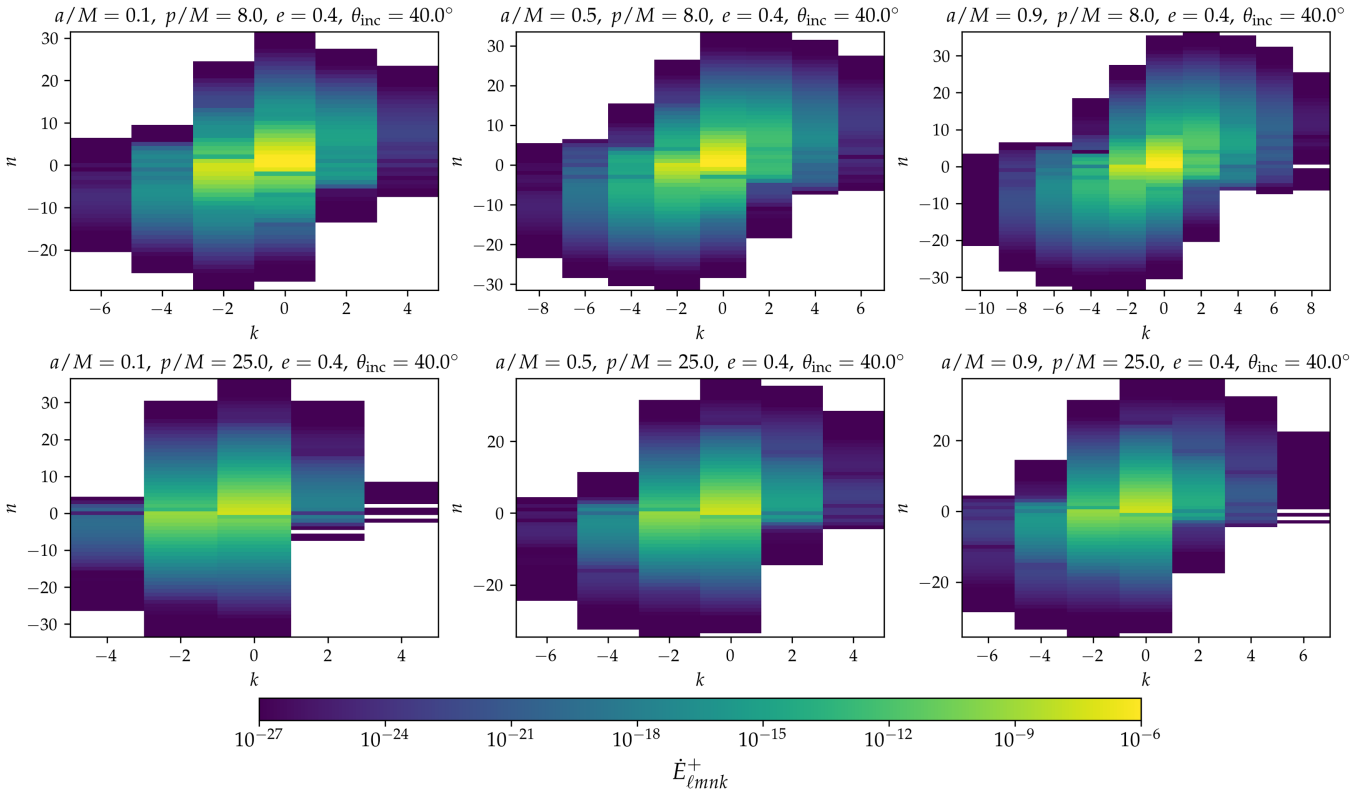


FIG. 12. Multipolar (n,k) components of the scalar spectra, $\dot{E}^{+}_{\ell mnk}$, at infinity for varying a/M and p/M, with fixed $e = 0.4$, $\theta_{\rm inc} = 40°$, and $\ell = m = 1$. The color scale indicates the magnitude of the single-mode flux.

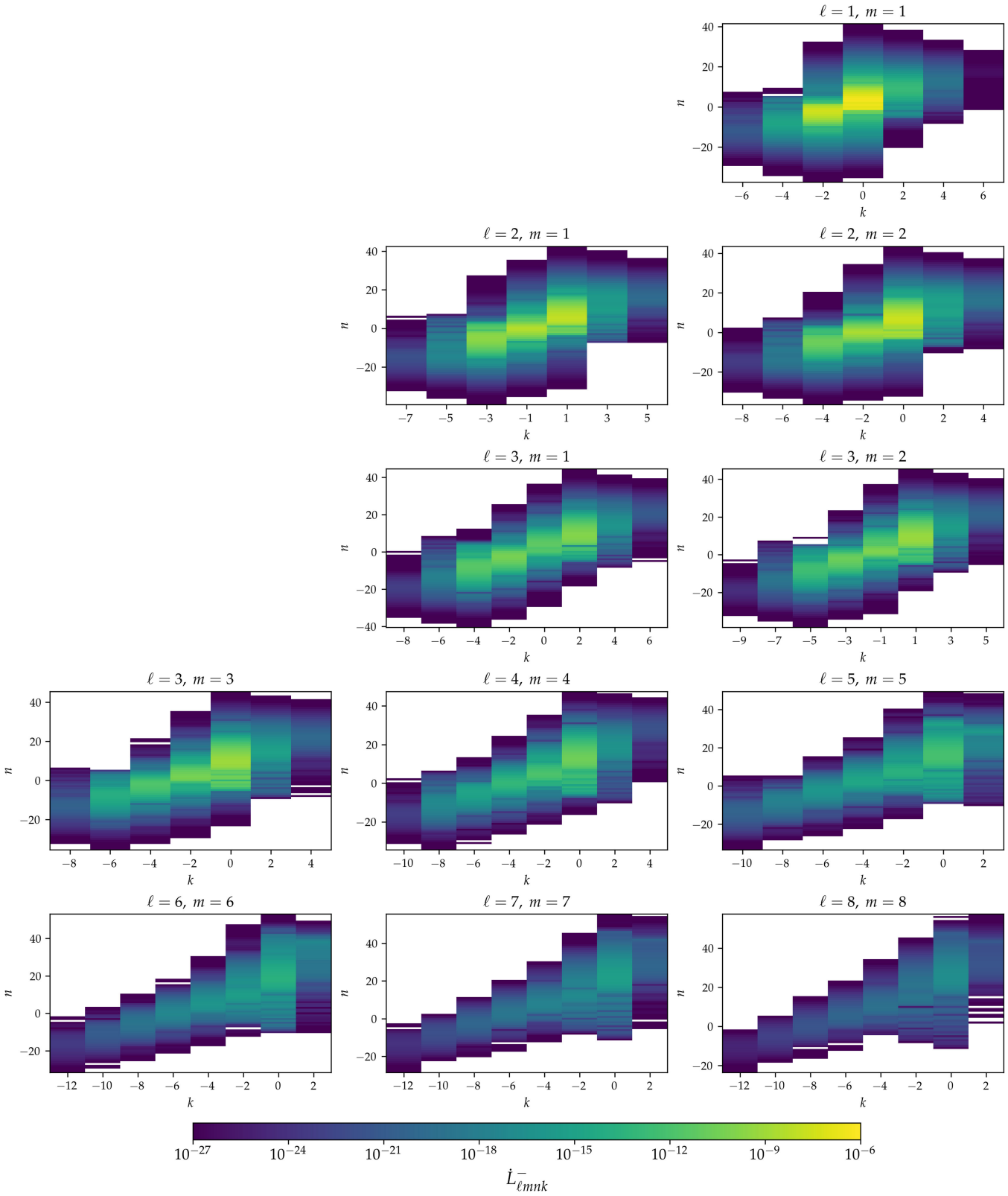


FIG. 13. Multipolar (n, k) components of the scalar spectra, $\dot{L}^{-}_{\ell mnk}$, at the horizon for varying ℓ and m, with fixed $a/M = 0.3$, $p/M = 7$, $e = 0.5$, and $\theta_{\rm inc} = 30°$. The color scale indicates the magnitude of the single-mode flux.

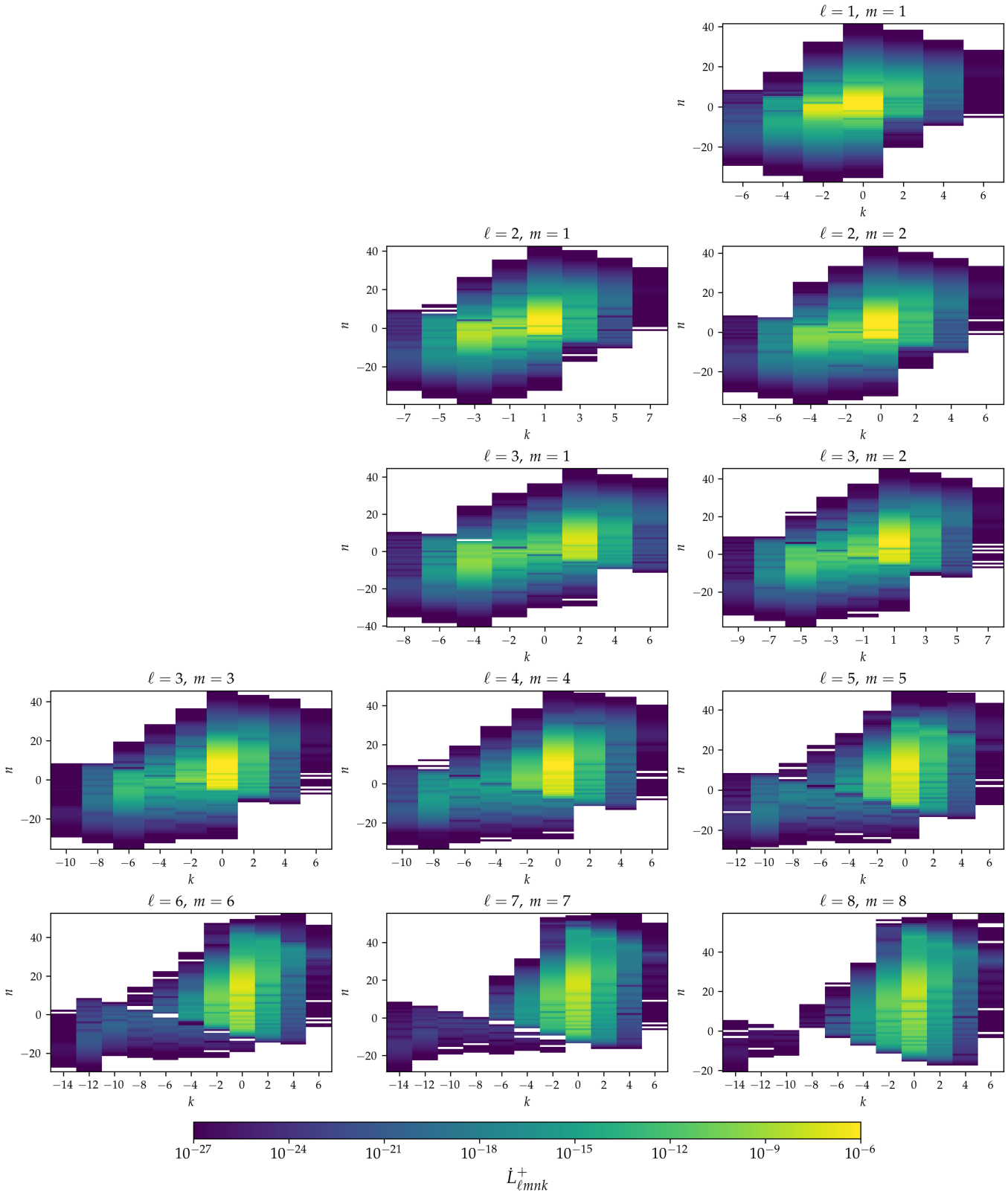


FIG. 14. Multipolar (n, k) components of the scalar spectra, $\dot{L}^{+}_{\ell mnk}$, at infinity for varying ℓ and m, with fixed $a/M = 0.3$, $p/M = 7$, $e = 0.5$, and $\theta_{\rm inc} = 30°$. The color scale indicates the magnitude of the single-mode flux.

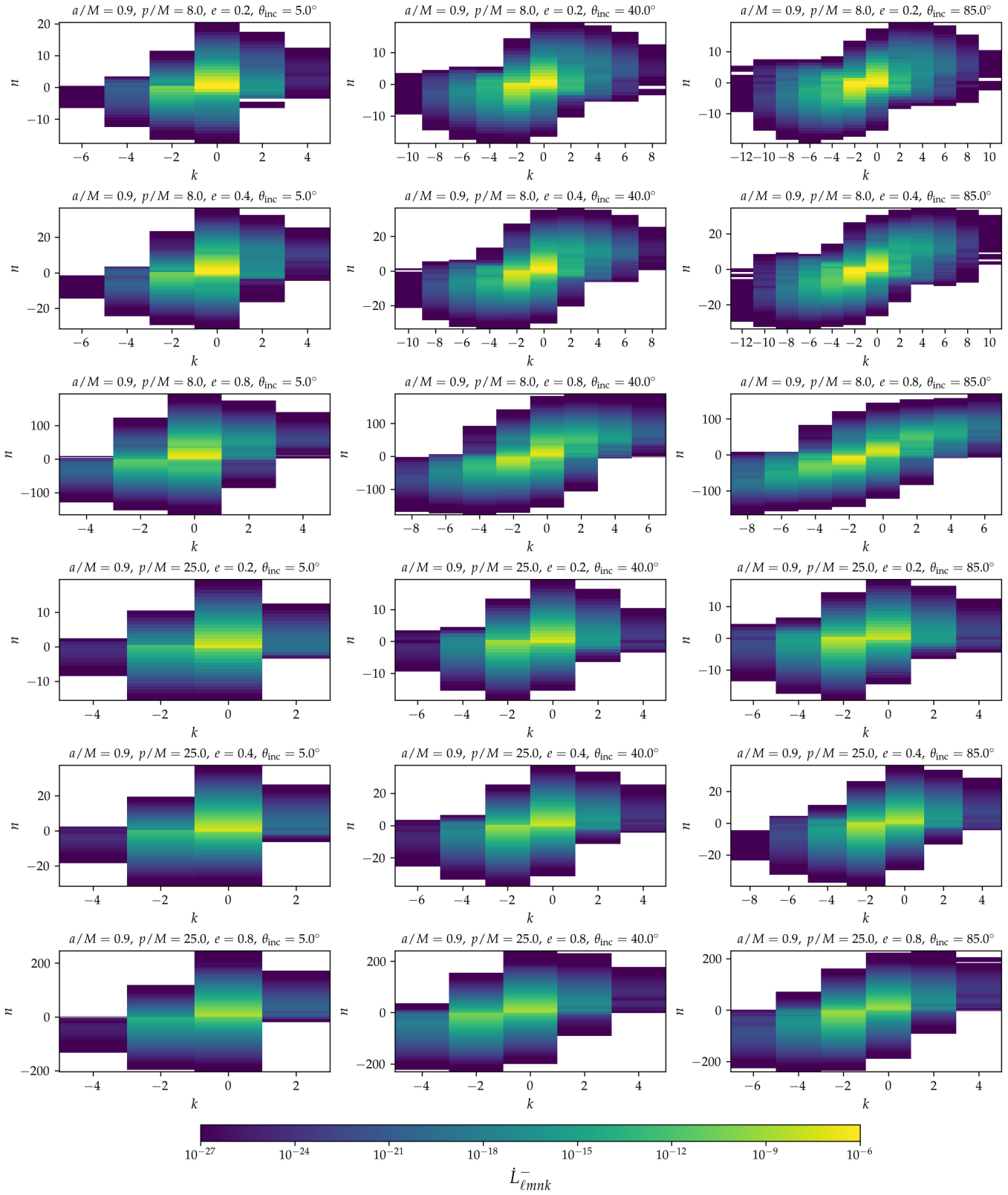


FIG. 15. Multipolar (n, k) components of the scalar spectra, $\dot{L}^{-}_{\ell mnk}$, at the horizon for varying p/M, e, and $\theta_{\rm inc}$, with fixed $a/M = 0.9$ and $\ell = m = 1$. The color scale indicates the magnitude of the single-mode flux.

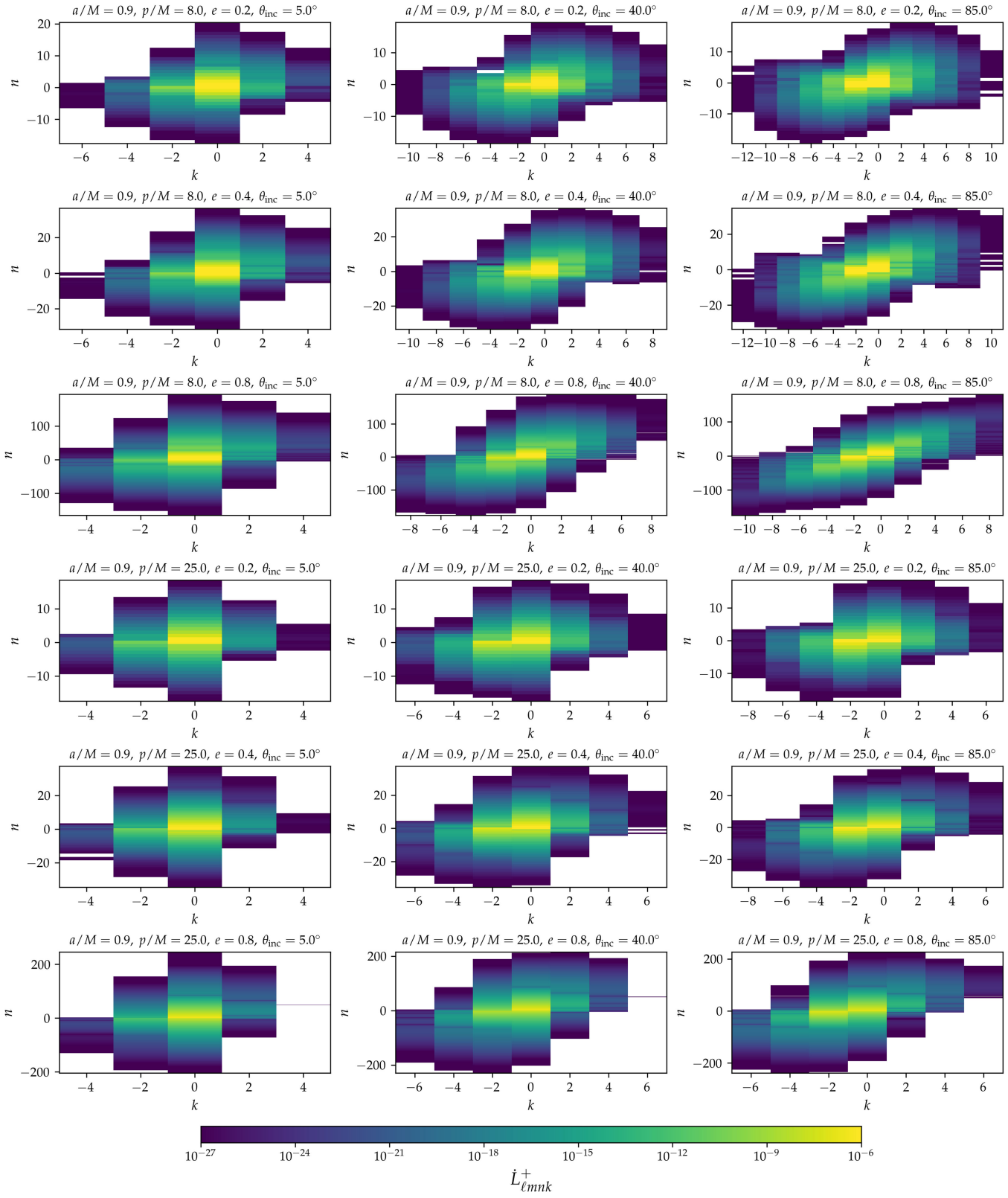


FIG. 16. Multipolar (n, k) components of the scalar spectra, $\dot{L}^{+}_{\ell mnk}$, at infinity for varying p/M, e, and $\theta_{\rm inc}$, with fixed $a/M = 0.9$ and $\ell = m = 1$. The color scale indicates the magnitude of the single-mode flux.

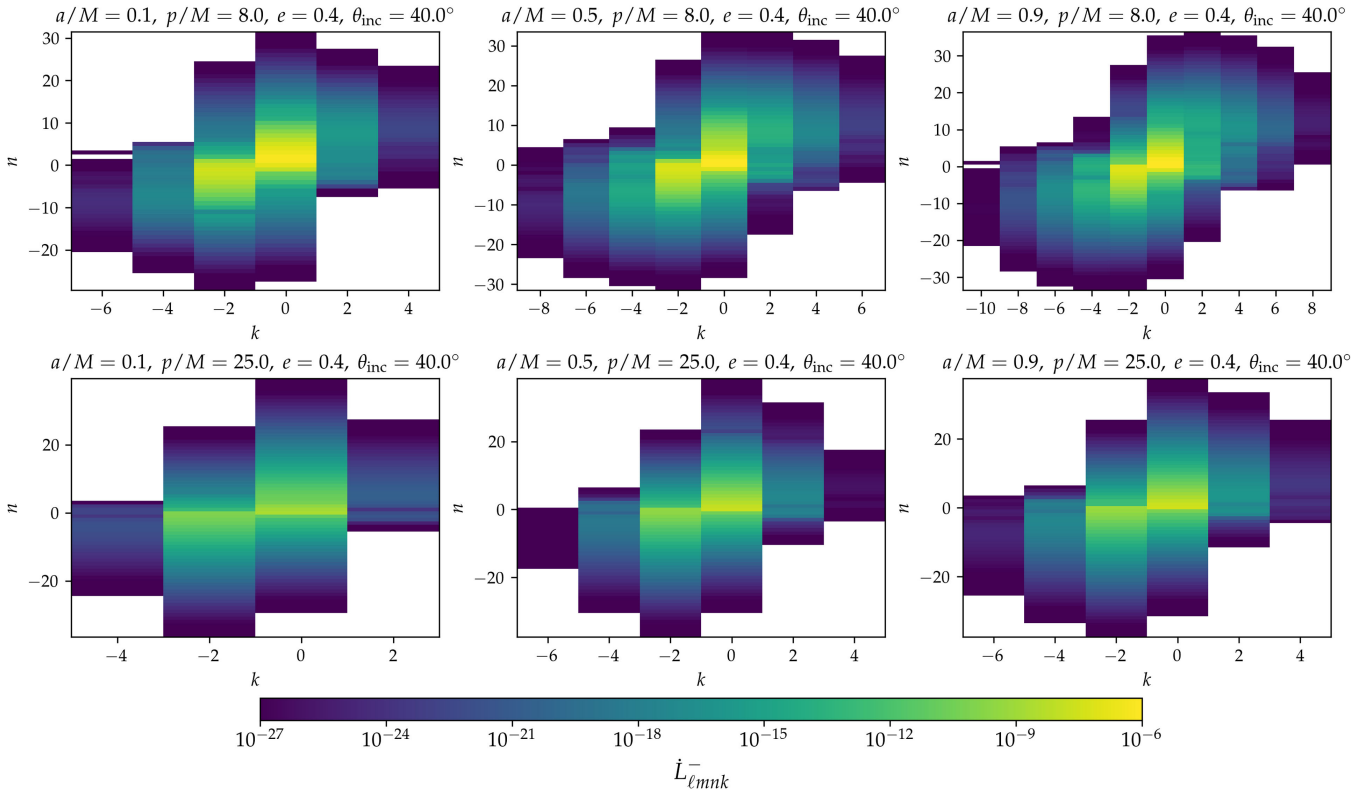


FIG. 17. Multipolar (n,k) components of the scalar spectra, $\dot{L}^{-}_{\ell mnk}$, at the horizon for varying a/M and p/M, with fixed $e = 0.4$, $\theta_{\rm inc} = 40°$, and $\ell = m = 1$. The color scale indicates the magnitude of the single-mode flux.

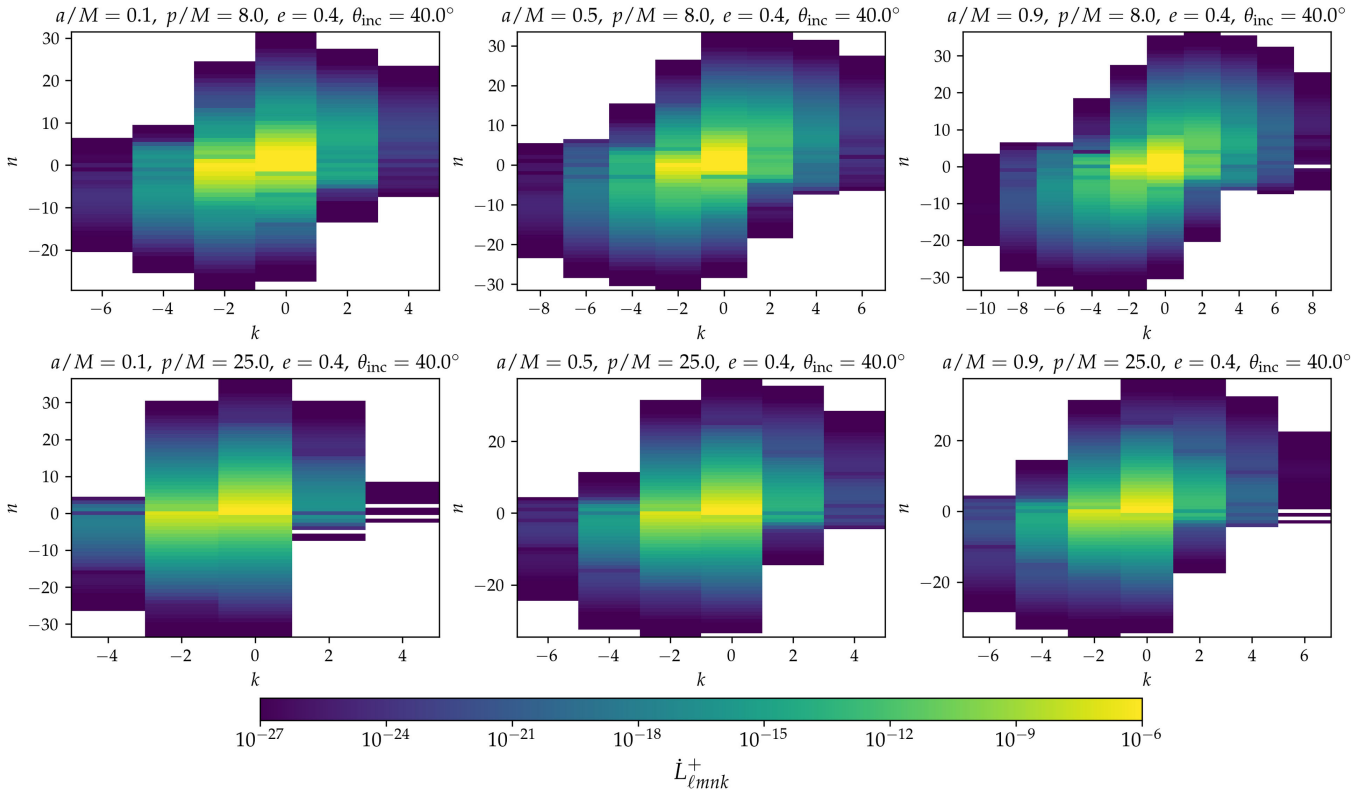


FIG. 18. Multipolar (n,k) components of the scalar spectra, $\dot{L}^{+}_{\ell mnk}$, at infinity for varying a/M and p/M, with fixed $e = 0.4$, $\theta_{\rm inc} = 40°$, and $\ell = m = 1$. The color scale indicates the magnitude of the single-mode flux.

[1] A. G. Abac *et al.* (LIGO Scientific Collaboration, VIRGO Collaboration, and KAGRA Collaboration), Astrophys. J. Lett. **1004**, L22 (2026).
[2] R. Abbott *et al.* (LIGO Scientific Collaboration, VIRGO Collaboration, and KAGRA Collaboration), Phys. Rev. D **112**, 084080 (2025).
[3] R. Abbott *et al.* (LIGO Scientific Collaboration and Virgo Collaboration), Phys. Rev. D **102**, 043015 (2020).
[4] R. Abbott *et al.* (LIGO Scientific Collaboration and Virgo Collaboration), Astrophys. J. Lett. **896**, L44 (2020).
[5] N. Yunes and X. Siemens, Living Rev. Relativity **16**, 9 (2013).
[6] E. M. Sänger *et al.*, Phys. Rev. D **113**, 084070 (2026).
[7] B. Gao, S.-P. Tang, H.-T. Wang, J. Yan, and Y.-Z. Fan, Phys. Rev. D **110**, 044022 (2024).
[8] M. Punturo *et al.*, Classical Quantum Gravity **27**, 194002 (2010).
[9] S. Dwyer, D. Sigg, S. W. Ballmer, L. Barsotti, N. Mavalvala, and M. Evans, Phys. Rev. D **91**, 082001 (2015).
[10] P. Amaro-Seoane *et al.* (LISA Collaboration), arXiv:1702.00786.
[11] J. Mei *et al.* (TianQin Collaboration), Prog. Theor. Exp. Phys. **2021**, 05A107 (2021).
[12] P. Ajith *et al.*, J. Cosmol. Astropart. Phys. 01 (2025) 108.
[13] A. Abac *et al.* (ET Collaboration), J. Cosmol. Astropart. Phys. 03 (2026) 081.
[14] M. Colpi *et al.* (LISA Collaboration), arXiv:2402.07571.
[15] L. Barack *et al.*, Classical Quantum Gravity **36**, 143001 (2019).
[16] K. G. Arun *et al.* (LISA Collaboration), Living Rev. Relativity **25**, 4 (2022).
[17] B. S. Sathyaprakash *et al.*, arXiv:1903.09221.
[18] S. Babak, J. Gair, A. Sesana, E. Barausse, C. F. Sopuerta, C. P. L. Berry, E. Berti, P. Amaro-Seoane, A. Petiteau, and A. Klein, Phys. Rev. D **95**, 103012 (2017).
[19] C. E. A. Chapman-Bird *et al.*, Phys. Rev. D **112**, 104023 (2025).
[20] A. Cárdenas-Avendaño and C. F. Sopuerta, Testing Gravity with Extreme-Mass-Ratio Inspirals, In *Recent Progress on Gravity Tests*, Springer Series in Astrophysics and Cosmology (Springer, Singapore, 2024).
[21] E. Barausse *et al.*, Gen. Relativ. Gravit. **52**, 81 (2020).
[22] E. Barausse, N. Yunes, and K. Chamberlain, Phys. Rev. Lett. **116**, 241104 (2016).
[23] J. L. Blázquez-Salcedo, C. F. B. Macedo, V. Cardoso, V. Ferrari, L. Gualtieri, F. S. Khoo, J. Kunz, and P. Pani, Phys. Rev. D **94**, 104024 (2016).
[24] K. Glampedakis and S. Babak, Classical Quantum Gravity **23**, 4167 (2006).
[25] L. Barack and C. Cutler, Phys. Rev. D **75**, 042003 (2007).
[26] V. Cardoso, G. Castro, and A. Maselli, Phys. Rev. Lett. **121**, 251103 (2018).
[27] S. Datta, R. Brito, S. Bose, P. Pani, and S. A. Hughes, Phys. Rev. D **101**, 044004 (2020).
[28] P. Pani and A. Maselli, Int. J. Mod. Phys. D **28**, 1944001 (2019).
[29] E. Maggio, M. van de Meent, and P. Pani, Phys. Rev. D **104**, 104026 (2021).
[30] K. Destounis, A. G. Suvorov, and K. D. Kokkotas, Phys. Rev. D **102**, 064041 (2020).
[31] G. A. Piovano, A. Maselli, and P. Pani, Phys. Lett. B **811**, 135860 (2020).
[32] N. Sago and T. Tanaka, Phys. Rev. D **104**, 064009 (2021).
[33] G. A. Piovano, A. Maselli, and P. Pani, Phys. Rev. D **107**, 024021 (2023).
[34] L. G. Collodel, D. D. Doneva, and S. S. Yazadjiev, Phys. Rev. D **105**, 044036 (2022).
[35] L. Barack and A. Pound, Rep. Prog. Phys. **82**, 016904 (2019).
[36] A. Pound, B. Wardell, N. Warburton, and J. Miller, Phys. Rev. Lett. **124**, 021101 (2020).
[37] N. Warburton, A. Pound, B. Wardell, J. Miller, and L. Durkan, Phys. Rev. Lett. **127**, 151102 (2021).
[38] B. Wardell, A. Pound, N. Warburton, J. Miller, L. Durkan, and A. Le Tiec, Phys. Rev. Lett. **130**, 241402 (2023).
[39] P. Wagle, D. Li, Y. Chen, and N. Yunes, Phys. Rev. D **109**, 104029 (2024).
[40] D. Li, P. Wagle, Y. Chen, and N. Yunes, Phys. Rev. X **13**, 021029 (2023).
[41] A. Maselli, N. Franchini, L. Gualtieri, and T. P. Sotiriou, Phys. Rev. Lett. **125**, 141101 (2020).
[42] A. Spiers, A. Maselli, and T. P. Sotiriou, Phys. Rev. D **109**, 064022 (2024).
[43] S. Barsanti, N. Franchini, L. Gualtieri, A. Maselli, and T. P. Sotiriou, Phys. Rev. D **106**, 044029 (2022).
[44] C. Zhang, Y. Gong, D. Liang, and B. Wang, J. Cosmol. Astropart. Phys. 06 (2023) 054.
[45] M. Della Rocca, S. Barsanti, L. Gualtieri, and A. Maselli, Phys. Rev. D **109**, 104079 (2024).
[46] T. Zi and S. Kumar, J. Cosmol. Astropart. Phys. 04 (2026) 074.
[47] A. Roy, L. Küchler, A. Pound, and R. Panosso Macedo, Phys. Rev. Lett. **136**, 251404 (2026).
[48] S. Barsanti, A. Maselli, T. P. Sotiriou, and L. Gualtieri, Phys. Rev. Lett. **131**, 051401 (2023).
[49] M. Della Rocca, G. Antoniou, L. Gualtieri, and A. Maselli, Phys. Rev. D **112**, 024042 (2025).
[50] C. Zhang, H. Guo, Y. Gong, and B. Wang, J. Cosmol. Astropart. Phys. 06 (2023) 020.
[51] T. Zi, P.-C. Li, B.-M. Gu, and F.-W. Shu, J. Cosmol. Astropart. Phys. 04 (2026) 077.
[52] T. Zi and F.-W. Shu, Eur. Phys. J. C **85**, 1251 (2025).
[53] A. Maselli, N. Franchini, L. Gualtieri, T. P. Sotiriou, S. Barsanti, and P. Pani, Nat. Astron. **6**, 464 (2022).
[54] L. Speri, S. Barsanti, A. Maselli, T. P. Sotiriou, N. Warburton, M. van de Meent, A. J. K. Chua, O. Burke, and J. Gair, Phys. Rev. D **113**, 023036 (2026).
[55] N. Warburton and L. Barack, Phys. Rev. D **81**, 084039 (2010).
[56] N. Warburton and L. Barack, Phys. Rev. D **83**, 124038 (2011).
[57] N. Warburton, Phys. Rev. D **91**, 024045 (2015).
[58] Z. Nasipak, T. Osburn, and C. R. Evans, Phys. Rev. D **100**, 064008 (2019).
[59] STORM, https://github.com/saragliorio/STORM.
[60] M. Saravani and T. P. Sotiriou, Phys. Rev. D **99**, 124004 (2019).

[61] T. Damour and G. Esposito-Farese, Phys. Rev. Lett. **70**, 2220 (1993).
[62] D. D. Doneva and S. S. Yazadjiev, Phys. Rev. Lett. **120**, 131103 (2018).
[63] H. O. Silva, J. Sakstein, L. Gualtieri, T. P. Sotiriou, and E. Berti, Phys. Rev. Lett. **120**, 131104 (2018).
[64] A. Dima, E. Barausse, N. Franchini, and T. P. Sotiriou, Phys. Rev. Lett. **125**, 231101 (2020).
[65] C. A. R. Herdeiro, E. Radu, H. O. Silva, T. P. Sotiriou, and N. Yunes, Phys. Rev. Lett. **126**, 011103 (2021).
[66] D. D. Doneva, F. M. Ramazanoğlu, H. O. Silva, T. P. Sotiriou, and S. S. Yazadjiev, Rev. Mod. Phys. **96**, 015004 (2024).
[67] S. Alexander and N. Yunes, Phys. Rep. **480**, 1 (2009).
[68] N. Yunes and L. C. Stein, Phys. Rev. D **83**, 104002 (2011).
[69] D. M. Eardley, Astrophys. J. **196**, L59 (1975).
[70] T. Damour and G. Esposito-Farese, Classical Quantum Gravity **9**, 2093 (1992).
[71] F.-L. Julié, Phys. Rev. D **97**, 024047 (2018).
[72] J. E. Chase, Commun. Math. Phys. **19**, 276 (1970).
[73] S. W. Hawking, Commun. Math. Phys. **25**, 167 (1972).
[74] J. D. Bekenstein, Phys. Rev. D **51**, R6608 (1995).
[75] T. P. Sotiriou and V. Faraoni, Phys. Rev. Lett. **108**, 081103 (2012).
[76] L. Hui and A. Nicolis, Phys. Rev. Lett. **110**, 241104 (2013).
[77] R. Nair, S. Perkins, H. O. Silva, and N. Yunes, Phys. Rev. Lett. **123**, 191101 (2019).
[78] H. O. Silva, A. M. Holgado, A. Cárdenas-Avendaño, and N. Yunes, Phys. Rev. Lett. **126**, 181101 (2021).
[79] A. Saffer and K. Yagi, Phys. Rev. D **104**, 124052 (2021).
[80] Z. Lyu, N. Jiang, and K. Yagi, Phys. Rev. D **105**, 064001 (2022); **106**, 069901(E) (2022).
[81] T. P. Sotiriou and S.-Y. Zhou, Phys. Rev. D **90**, 124063 (2014).
[82] T. P. Sotiriou and S.-Y. Zhou, Phys. Rev. Lett. **112**, 251102 (2014).
[83] F. Thaalba, G. Antoniou, and T. P. Sotiriou, Classical Quantum Gravity **40**, 155002 (2023).
[84] B. Carter, Phys. Rev. **174**, 1559 (1968).
[85] V. Ferrari, L. Gualtieri, and P. Pani, *General Relativity and its Applications* (CRC Press, Boca Raton, FL, 2021).
[86] Y. Mino, M. Sasaki, M. Shibata, H. Tagoshi, and T. Tanaka, Prog. Theor. Phys. Suppl. **128**, 1 (1997).
[87] S. Chandrasekhar, *The Mathematical Theory of Black Holes* (Oxford University Press, New York, 1985).
[88] M. van de Meent, Classical Quantum Gravity **37**, 145007 (2020).
[89] S. A. Teukolsky, Astrophys. J. **185**, 635 (1973).
[90] S. Drasco, E. E. Flanagan, and S. A. Hughes, Classical Quantum Gravity **22**, S801 (2005).
[91] S. Isoyama, R. Fujita, H. Nakano, N. Sago, and T. Tanaka, Prog. Theor. Exp. Phys. **2013**, 063E01 (2013).
[92] U. Ruangsri and S. A. Hughes, Phys. Rev. D **89**, 084036 (2014).
[93] P. Lynch, V. Witzany, M. van de Meent, and N. Warburton, Classical Quantum Gravity **41**, 225002 (2024).
[94] Z. Nasipak and C. R. Evans, Phys. Rev. D **104**, 084011 (2021).
[95] Boost C++ libraries, https://www.boost.org.
[96] S. A. Hughes, N. Warburton, G. Khanna, A. J. K. Chua, and M. L. Katz, Phys. Rev. D **103**, 104014 (2021); **107**, 089901(E) (2023).
[97] A. J. K. Chua, M. L. Katz, N. Warburton, and S. A. Hughes, Phys. Rev. Lett. **126**, 051102 (2021).
[98] M. L. Katz, A. J. K. Chua, L. Speri, N. Warburton, and S. A. Hughes, Phys. Rev. D **104**, 064047 (2021).
[99] L. Speri, M. L. Katz, A. J. K. Chua, S. A. Hughes, N. Warburton, J. E. Thompson, C. E. A. Chapman-Bird, and J. R. Gair, Front. Appl. Math. Stat. **9**, 1266739 (2024).
[100] R. Fujita and H. Tagoshi, Prog. Theor. Phys. **112**, 415 (2004).
[101] M. Casals, A. C. Ottewill, and N. Warburton, Proc. R. Soc. A **475**, 20180701 (2019).
[102] S. A. Hughes, Phys. Rev. D **61**, 084004 (2000).
[103] G. H. Golub and C. F. V. Loan, *Matrix Computations*, 4th ed. (Johns Hopkins University Press, Baltimore, 2013).
[104] E. W. Leaver, Proc. R. Soc. A **402**, 285 (1985).
[105] S. Mano, H. Suzuki, and E. Takasugi, Prog. Theor. Phys. **95**, 1079 (1996).
[106] M. Sasaki and H. Tagoshi, Living Rev. Relativity **6**, 6 (2003).
[107] Z. Nasipak, Classical Quantum Gravity **42**, 165001 (2025).
[108] A. Zenginoğlu, Phys. Rev. D **83**, 127502 (2011).